https://doi.org/10.5194/egusphere-2025-5958
Preprint. Discussion started: 3 February 2026

Development of ECCO-downscaled Amundsen-Bellingshausen Sea regional simulation using MITgcm(66j)

Yoshihiro Nakayama[1], Shuntaro Hyogo[2], Yichen Lin[3], Taewook Park[4], Jinho Lee[4], Justine Caillet[1], Gobishankar Mohan[1], Mattia Poinelli[5,6], Pierre Dutrieux[7], Kazuki Nakata[8], Hong Zhang[6], Brice Loose[9], and Lauren Kowalski[9]

[1]Thayer School of Engineering, Dartmouth College, Hanover, NH, USA
[2]Institute of Low Temperature Science, Hokkaido University, Sapporo, Japan
[3]School of Atmospheric Sciences, Sun Yat-sen University, and Southern Marine Science and Engineering Guangdong Laboratory (Zhuhai), 519082, Zhuhai, China
[4]Division of Ocean and Atmosphere Sciences, Korea Polar Research Institute, Incheon 21990, Republic of Korea
[5]Deaprtment of Earth System Science, University of California, Irvine, CA
[6]Jet Propulsion Laboratory, California Institute of Technology, Pasadena, CA.
[7]British Antarctic Survey, Natural Environment Research Council, Cambridge, UK
[8]Earth Observation Research Center, Japan Aerospace Exploration Agency, Tsukuba, Japan
[9]Graduate School of Oceanography, University of Rhode Island, Narragansett, RI USA

Correspondence: Y. Nakayama (Yoshihiro.Nakayama@dartmouth.edu)

Abstract. The Amundsen and Bellingshausen Seas are among the most rapidly changing regions of the Southern Ocean, playing a pivotal role in Antarctic ice-shelf mass loss and global sea-level rise. Several ocean models have been developed to investigate these changes, revealing complex interactions among the atmosphere, ocean, sea ice, and ice shelves. However, the diversity of model configurations, parameter choices, and model versions often hampers user-friendliness, limits meaningful intercomparison, and constrains broader multidisciplinary use. Here, we present a regional ocean model configuration of the Amundsen and Bellingshausen Seas with a horizontal resolution of 2.2-3.9 km based on MITgcm, downscaled from the global ECCO-LLC270 ocean state estimate, and further optimized using regional observations. We conduct extensive model evaluation and demonstrate its applications through multiple examples and previously published analyses, with the goal of providing model configuration and their outputs - achieving good model-data agreement - to the broad scientific community. The model reproduces key hydrographic features of the region, including realistic temperature and salinity profiles and water mass distributions that closely align with local CTD and mooring observations. Simulated sea-ice concentration and extent are consistent with satellite observations, capturing the observed seasonal cycle and spatial variability. Ice-shelf basal melt rates fall within the range of available satellite and in situ estimates. The configuration also includes passive tracers for surface water, ice-shelf meltwater, and Circumpolar Deep Water, as well as Lagrangian particle-tracking capabilities that facilitate studies of water-mass transformation and tracer pathways. By providing open access to the model code, configuration, diagnostics, tracer outputs, and sensitivity experiments, we aim to support data interpretation, hypothesis testing, and observational planning across the broad scientific community.

https://doi.org/10.5194/egusphere-2025-5958
Preprint. Discussion started: 3 February 2026

1 Introduction

The Amundsen Sea (AS) and Bellingshausen Sea (BS) are among the most critical regions in Antarctica in terms of ice-shelf change, where rapid thinning and basal melting have been observed over the past ∼20 years (Depoorter et al., 2013; Rignot et al., 2013; Paolo et al., 2015). These changes contribute substantially to ocean freshening and global sea-level rise through enhanced discharge of grounded ice (Shepherd et al., 2012; Rignot et al., 2013). The primary driver of high basal melt rates in both regions is the intrusion of relatively warm modified Circumpolar Deep Water (mCDW, approximately 0.5–1.5°C), which travels to ice-shelf cavities through glacially carved troughs from the continental shelf break at depths below ∼300–500 m (e.g., Jacobs et al., 1996; Nakayama et al., 2013; Dutrieux et al., 2014; Webber et al., 2017; Jenkins et al., 2018).

In recent years, multiple research groups have developed regional ocean models for the AS and BS to resolve key processes such as mCDW inflow, ice-shelf–ocean interactions, and cross-shelf processes. These efforts have yielded valuable insights into the dynamics and variability of warm-water intrusions across a range of spatial and temporal scales. Several studies have examined historical and projected changes in the Amundsen Sea (e.g., Thoma et al., 2008; Assmann et al., 2013; Kimura et al., 2017; Nakayama et al., 2017; Naughten et al., 2022; Jourdain et al., 2022; Naughten et al., 2023; Park et al., 2024; O'Connor et al., 2025), while others have explored diverse aspects of the regional system, including mCDW and glacial meltwater transport (e.g., Nakayama et al., 2014a, 2019; Hyogo et al., 2024; Shrestha et al., 2024; St-Laurent et al., 2024), biogeochemical–ocean interactions (e.g., St-Laurent et al., 2017, 2019), and coupled ice–ocean dynamics (e.g., De Rydt et al., 2014; Donat-Magnin et al., 2021; Caillet et al., 2023). Despite these advances, model configurations and sets of parameters differ widely (even including those published by the same group using the same configurations) in their representations of bathymetry, surface forcing, boundary conditions, and subgrid-scale parameterizations (e.g., mixing, tides, and ice-shelf melting). As a result, model outputs are difficult to cross-compare, even when addressing similar research questions. This diversity in model design poses challenges for reproducibility and makes it difficult for non-specialists to use ocean model results to complement their own research, limiting their broader applicability to disciplines such as ocean data analyses, glaciology, biogeochemistry, paleoceanography, and observational planning.

Over the past decade, our research group has focused on hindcast simulations that achieve close agreement with observations using the Massachusetts Institute of Technology general circulation model (MITgcm). This work includes downscaling the global ECCO (Estimating the Circulation and Climate of the Ocean)-LLC270 ocean state estimate (Zhang et al., 2018) and developing regional ocean state estimates with optimized parameters (e.g., Nakayama et al., 2017, 2018, 2021b). Building on this foundation, the latest version of the MITgcm-based AS and BS regional simulation reproduces the mean hydrographic structure, seasonal to interannual variability in thermocline depth, ocean heat intrusions, and key physical processes driving ice-shelf melting, in good agreement with observations (Nakayama et al., 2018; Hyogo et al., 2024; Park et al., 2024). To further advance scientific understanding and maximize the impact of regional modeling, we believe a standardized configuration that promotes transparency, comparability, and collaboration is necessary.

Here, we present a comprehensive evaluation of the ECCO-downscaled Amundsen-Bellingshausen Sea simulation, based on the model configuration developed by Nakayama et al. (2018) and further refined by Hyogo et al. (2024) and Park et al.

https://doi.org/10.5194/egusphere-2025-5958
Preprint. Discussion started: 3 February 2026

(2024). We assess model performance in diverse aspects, including sea ice, ocean, and ice-shelf melting. In addition, we introduce a suite of tools and example applications for conducting sensitivity experiments, passive tracer simulations, and Lagrangian particle tracking, as well as providing examples from past studies that rely on this framework. These tools support post-simulation oceanographic analysis, process-oriented studies, and observational planning.

2 Methods

2.1 Ocean model

We design a regional ocean simulation using a configuration of the MITgcm version 66j for the AS and BS (Fig. 1). The model configuration is based on Nakayama et al. (2018); Hyogo et al. (2024); Park et al. (2024), but we extend the simulation period from January 1992 through April 2025. The model includes dynamic and thermodynamic sea-ice processes (Losch et al., 2010) and thermodynamic ice-shelf interactions (Losch, 2008). The model domain encompasses the AS and BS (indicated by the black line in Fig. 1 inset). The model uses a latitude–longitude grid north of 70 °S and a bipolar grid south of 70 °S (see Forget et al. (2015) for details) with a horizontal grid spacing in the AS and BS of 2.2–3.9 km. The vertical discretization comprises 70 levels varying in thickness from 10 m near the surface, 70–90 m at depths of 500–1000 m, and 450 m at the deepest level of 6000 m. The model bathymetry is based on the International Bathymetric Chart of the Southern Ocean (IBCSO) (Arndt et al., 2013), and the model ice draft and bathymetry under the ice shelves are based on Bed-Machine Antarctica v3 (Morlighem, 2022). The initial conditions are derived from a 16-year (2001–2016) spin-up, integrated from rest and from the January World Ocean Atlas 2009 temperature (Locarnini et al., 2010) and salinity (Antonov et al., 2010) fields. Surface forcing for the 1992–2017 period is provided by ECCO (Estimating the Circulation and Climate of the Ocean)-LLC270 (Zhang et al., 2018), which is based on ERA-Interim (Dee et al., 2011) and has been adjusted using the ECCO adjoint model-based methodology (Wunsch and Heimbach, 2013). For the extension period (ie, 2018 and onward), ECCO-LLC270 computed the time mean seasonal cycle of atmospheric forcing adjustments from 1992 to 2017 and applied those results to ERA5 reanalysis for forcing fields. Similarly, the boundary conditions for the 1992-2017 and 2018-2025 periods are provided by ECCO-LLC270 and ECCO-LLC270 extension, respectively. This model does not account for tidal forcing. We assume steady-state ice-shelf thickness and cavity geometry, and compute basal mass loss rates following the three equations formulation of Hellmer and Olbers (1989) as refined by Holland and Jenkins (1999). Because cavity geometry and ocean circulation are not well resolved with 3-4 km horizontal resolution, we do not allow the heat and salt transfer coefficients to vary with friction velocity. Instead, we prescribe constant values of $0.25 \times 10^{-4}\ m\ s^{-1}$ for George VI and $0.5 \times 10^{-4}\ m\ s^{-1}$ for all other ice shelves (Table S3 in Hyogo et al. (2024)). Several icebergs are grounded off the Bear Peninsula along the 400 m isobath, forming a barrier of grounded icebergs and landfast ice that limits sea-ice transport between the eastern and central Amundsen Sea. Following Nakayama et al. (2017), we represent this region as a 10-m ice shelf to represent a barrier to improve simulated sea ice dynamics. No iceberg melting parameterization is applied.

https://doi.org/10.5194/egusphere-2025-5958
Preprint. Discussion started: 3 February 2026

2.2 Observations used for evaluation

For sea ice, we use sea-ice concentration (SIC) data from the Bootstrap Sea Ice Concentrations from Nimbus-7 SMMR and DMSP SSM/I–SSMIS, Version 4 product provided by the National Snow and Ice Data Center (NSIDC) (Comiso, 2023). The dataset has a daily resolution of 25 km. Sea-ice thickness is taken from the SMOS-derived Antarctic sea-ice thickness product for 2010–2020 generated by the Alfred Wegener Institute (AWI) (Tian-Kunze and Kaleschke, 2021). This dataset has a daily resolution of 12.5 km and covers 15 April–15 October each year; thickness estimates below 1 m are considered reliable (Kaleschke et al., 2024). Observation-based polynya areas are obtained from the Daily Edge of Each Polynya in Antarctic (DEEP-AA) dataset (Lin et al., 2024a), which has a 6.25 km daily resolution and covers April–October. Based on SIC data retrieved with the Advanced Microwave Scanning Radiometer (AMSR) on board of NASA's Terra and Aqua satellites, DEEP-AA identifies regions of open water where SIC is less than 0.8, while its reliability has been validated (Lin et al., 2024b). Daily sea-ice production (SIP) is taken from Nakata and Ohshima (2022), which derives SIP from AMSR brightness temperatures combined with meteorological forcing from the ERA5 reanalysis. This product has a 12.5 km daily resolution. Half-monthly landfast ice extent is obtained from the Circum-Antarctic Landfast Sea Ice Extent, 2000–2018, Version 2.2 dataset (Fraser et al., 2020).

For the ocean, we evaluate the model's ocean hydrography and circulation by comparing simulated hydrographic properties with ship-based CTD and mooring observations. For the ship-based observations, we used the measurements collected during several research cruises: R/V James Clark Ross cruise JR165 (20 March-27 March 2007) (Castro-Morales et al., 2013), the IBRV Araon ANA02C (16 February–4 March 2012) (Kim et al., 2017), ANA08B (18 January 2017–1 February 2018) (Assmann et al., 2019), R/V Nathaniel B. Palmer cruises NBP07-02 (19 February-6 March 2007) (Jacobs et al., 2012), NBP09-01 (13 January-29 January 2009) (Jacobs et al., 2011), and NBP19-01 (31 December 2018-6 January 2019) (Thompson et al., 2020). For the mooring, we also use an array of moored observations in the Eastern Amundsen Sea.The mooring observations are compiled for Pine Island Trough East (PITE), Pine Island Trough West (PITW), the middle of the Pine Island Trough (Mid-shelf), Pine Island Glacier front North (PIG_N), and Pine Island Glacier front South (PIG_S) as shown in Fig. 1. The oldest component of the record started in 2009, implemented by S. Jacobs. The timeseries was continued by the iSTAR program (A. Jenkins), and is now maintained as a UK long-term monitoring program. Each mooring is instrumented with 6 to 8 temperature sensors interspersed between the seabed and about 350m depth, resolving the structure of the warm bottom layer and the thermocline.

2.3 Passive Tracers

We include three passive tracers—surface-restoring, CDW, and ice-shelf-melt tracers—to facilitate the analysis of water-mass movement and transformation. For the surface-restoring tracer, the tracer concentration is restored to unity at the ocean surface everywhere except within 10 grid cells of the model boundary. Within this boundary region, the tracer is instead restored to zero to prevent artificial mixing of the surface-restoring tracer into deeper layers due to spurious mixing near the model boundary. For the CDW tracer, the model is initialized with a passive-tracer concentration of unity in regions where the

https://doi.org/10.5194/egusphere-2025-5958
Preprint. Discussion started: 3 February 2026

potential temperature exceeds 1.0 °C and north of the continental-shelf break. There is no additional forcing applied. Because the CDW tracer gradually mixes with surrounding water masses, we limit its output to a three-year period from 1992 to 1995. For the ice-shelf-melt tracer, the model is initialized with zero concentration, and tracer is released at the same rate as basal melt occurs at ice-shelf bases, following Nakayama et al. (2014a, 2017).

2.4 Particle release experiment

We carried out particle-release experiments using the Octopus package (https://github.com/jinbow/Octopus) in an offline configuration. Particles were released at selected locations and depths depending on the objective of each experiment. Both forward and backward integrations were performed using 5-daily mean outputs of ocean current: forward experiments examined the dispersion of water masses from specified release points, while backward experiments traced the origins of water entering key sites such as troughs and ice-shelf cavities. The overall approach follows earlier studies (Nakayama et al., 2019; Hyogo et al., 2024). The experiment can be easily adjusted for different release points, depths, or time periods. We also provide code, input, and particle experiments output as an example.

3 Model evaluation

3.1 Sea ice

3.1.1 Sea ice area

We evaluate the sea-ice area (SIA), defined as the sum of grid cell areas multiplied by their respective sea ice concentrations, considering only cells with at least 15%. The simulated monthly SIA time series agree well with observations (Figs. 2a-h and 3a). The simulated sea-ice concentration patterns for summer, autumn, winter, and spring are in agreement with observations (Figs. 2a-h). Qualitatively, the model reproduces the seasonal growth and expansion of sea ice during autumn and winter, the maximum extent and spatial distribution in winter, the presence of coastal polynyas, and the retreat during spring. However, summer sea ice concentration is underestimated. Observations show about 2.7×10^5 km^2 of sea ice remaining in the Amundsen Sea, whereas the simulation shows only about 0.5×10^5 km^2. To examine this further, we analyze detrended monthly anomalies in September and February (Figs. 3b–c). The simulation reproduces near-realistic anomaly evolution in September, but exhibits substantially larger variability than the observations for the February sea ice minimum. Whether in February or September, the SIA anomaly shows a significant correlation between the simulation and the observation (February: $r=0.39$, $p<0.05$; September: $r=0.77$, $p<0.05$), which demonstrates the reliable ability to reproduce the interannual variations of sea ice. For the seasonal cycle (Fig. 3d), the model shows that the SIA in winter is consistent with the observations, while in summer it is lower. From June to November, the uncertainty intervals (defined by one standard deviation) of the model and the observations overlap. Difficulties in simulating summer sea ice are common in other Antarctic continental simulations as well (e.g., Jourdain et al., 2017; Bett et al., 2020; Van Achter et al., 2022), likely due to challenges in representing sea ice dynamics—including fast ice and icebergs—as well as near-surface ocean stratification.

https://doi.org/10.5194/egusphere-2025-5958
Preprint. Discussion started: 3 February 2026

3.1.2 Sea-ice thickness

We perform a similar analysis for sea-ice thickness (Figs. 2i-l). Due to the limitations of remote sensing data, we only evaluate thin sea ice (<1 m) in the autumn and winter seasons. Qualitatively, simulated and observed sea-ice thickness distributions for autumn and winter are in good agreement with observations. In autumn, sea ice begins to thicken over the continental shelf, a feature captured in both the model and the observations. In winter, however, the model shows thick ice concentrated primarily over the continental shelf, whereas observations indicate thick ice not only over the shelf but also in the western part of the domain within the Ross Gyre. This discrepancy is likely due to the representation of sea-ice growing processes in the model as well as mismatches in the boundary conditions, with the advection of sea ice from the western boundary into the Ross Gyre being underestimated in our regional model. Similar to the results of SIC, the coastal polynyas with thinner ice are reproduced successfully.

3.1.3 Sea ice production and Polynya

Qualitatively, Amundsen, Pine Island Bay, and Bellingshausen polynyas are well represented in the simulation. For the Wrigley Gulf and Amundsen polynyas (Fig. 2), the simulated sea-ice formation rates for these regions agree closely with satellite-based estimates (Table 1). However, for the Pine Island Bay and Bellingshausen polynyas, the sea-ice production in the model is much larger than the observation, overestimated by 3.6 times and 5.9 times, respectively. The simulated lifespans of Pine Island Bay and Bellingshausen polynyas are in agreement with observations, but their areas are quite smaller (Figs. 4e-f and i-j). This indicates that simulated opening and closing of polynyas is reasonable and that the main error lies in the size of the polynyas during their maintenance period. A large amount of landfast ice surrounding these two polynyas is the likely reason for the overestimated sea-ice formation in the model compared to observation (Figs. 4a-b, Table 1). The landfast ice is not included in our model; this likely allows the simulated polynyas to expand more. For the Wrigley Gulf and Amundsen polynya (Figs. 4a-b), there is less landfast ice in the downstream (west side). Therefore, their area, lifespan, and ice production reproduced by our model are in good agreement with the observations (Figs. 4c-d and 4g-h). Particularly noteworthy is that the landfast ice located upstream (east side) of polynyas has been proven to be able to block the ice flow and play a promoting role in the polynya opening Ohshima et al. (2016). Our model established an “iceberg line” on the east side of the Amundsen polynya based on observations (Nakayama et al., 2014b, 2017), which played a crucial role in accurately reproducing the Amundsen polynya.

3.2 Ocean

Warm Circumpolar Deep Water (CDW) circulates through the Southern Ocean within the Antarctic Circumpolar Current and the Ross Gyre (Nakayama et al., 2018) as shown in Fig. 5. Some of this heat is transported onto the Amundsen and Bellingshausen Sea continental shelves. Once on the shelf, warm water follows glacially carved troughs for several hundred kilometers before entering ice-shelf cavities, as illustrated by the horizontal section at 545 m (Fig. 5b and Supplementary Movie 1 for the output from 2024 based on 5-daily mean). These intrusions of ocean heat are primarily driven by barotropic

https://doi.org/10.5194/egusphere-2025-5958
Preprint. Discussion started: 3 February 2026

currents that follow the glacial troughs (Fig. 5f). At shallower depths over the continental shelf, the coastal current generally flows westward from the Bellingshausen Sea toward the Amundsen Sea and exhibits a strong baroclinic structure (Fig. 5e). Near the surface, cold and fresh Winter Water (WW) accumulates due to surface cooling and meltwater input from ice shelves. This leads to a westward deepening of the thermocline across the continental shelf (Figs. 5a,c).

Here, we compare simulated ocean hydrography with ship-based (Figs. 6-8) and mooring (Figs. 9-10) observations across the AS and BS continental shelves (Fig. 1). We present several hydrographic cross-sections from the open ocean to ice-shelf cavities between 2007 and 2019, together with mooring time series, to evaluate simulated hydrographic structures and their temporal variability at locations where observations are available. Model fields are sampled from the same month as each observation to avoid comparing different phases of deep and shallow thermocline (lower and higher heat content) periods. In the Amundsen Sea, the first oceanographic observations were collected in 1994 (Jacobs et al., 1996). Since 2007, numerous observational campaigns have provided a broad view of water-mass distribution and variability, particularly in the eastern Amundsen Sea over the past two decades (e.g., Jacobs et al., 2011; Dutrieux et al., 2014; Heywood et al., 2016; Kim et al., 2016). Across these observations, no clear long-term trends in ocean properties and thermocline depths are evident; rather, the dominant signal is interannual to decadal variability in thermocline depth, with only minor changes in the characteristics of mCDW (Dutrieux et al., 2014; Webber et al., 2017).

3.2.1 Amundsen Sea

CTD observations

For the section from the open ocean leading to the Pine Island Ice Shelf (Figs. 1 and 6a-d), we observe intrusions of mCDW flowing toward the ice shelves. The upper layer is occupied by cold, relatively fresh WW, while mCDW fills the deeper layer, consistent with previous observations (Jacobs et al., 1996; Dutrieux et al., 2014). The simulated and observed thermocline in 2009 are located at approximately 200 m and 300-400 m depth, respectively (Figs. 6a-d). Observations and simulations show little bias in CDW properties. The simulated mCDW exhibits a maximum potential temperature bias of +0.15 °C, while the salinity shows no difference greater than 0.01 (Table 2).

For the section along the trough from open water leading to the Dotson Ice Shelf, observations reveal a two-layer structure of mCDW and WW, with the WW layer thicker than in the Eastern trough (Figs. 6a-h), consistent with the east-to-west thickening of WW (Figs. 5a-d). A typical characteristic of the mCDW intrusion in the Dotson Trough is its thin and highly modified structure, likely caused by the shallower trough bathymetry at the shelf break, which enhances the modification of CDW as it crosses the continental shelf. The connection between the glacially calved trough and open water is roughly 100 m shallower than the Eastern Trough. This enhanced modification is also captured in the simulation, although the model produces a thicker mCDW intrusion than observed, with observed and simulated thermocline depths located at 300-400 m and 500-600 m, respectively. The observed mCDW has a potential temperature of ∼0.5 °C and salinity of 34.65, making it colder and fresher than the mCDW in the eastern trough. In the simulation, mCDW intruding along the Dotson Trough is slightly warmer and more saline, with a potential temperature of ∼0.8 °C and salinity of 34.7. We also compare observed and simulated sections

https://doi.org/10.5194/egusphere-2025-5958
Preprint. Discussion started: 3 February 2026

for two different years, but no significant changes are found between the two years in either the observations or the simulations (Fig. S1).

Two sections connecting the open ocean to the Getz Ice Shelf are compared (Fig. 7). Observations along the Siple Trough reveal warm ocean heat intrusions from open water toward the Getz Ice Shelf. These intrusions consist of thin but warm mCDW, which is warmer and saltier than in the Dotson Trough by 0.32 °C and 0.02, respectively, based on their maximum temperature and salinity. The average thermocline depth is approximately 600 m. Despite the model showing qualitative agreement representing general features of mCDW intrusions, the simulated mCDW intrusion is too warm and saline with a shallower thermocline at ∼400 m. Further west, observations along the Western Getz Trough reveal warm ocean heat intrusions from open water toward the Getz Ice Shelf. These intrusions consist of thin but warm mCDW, which is warmer than in the Dotson Trough, accompanied by thickening WW and an average thermocline depth of approximately 600 m. The model reproduces these features, although the simulated mCDW intrusion is again too warm, too saline, and too thick, with a thermocline shallower at ∼400 m. For these two sections, we compare observed and simulated sections for two different years. No significant differences in mCDW temperature, salinity, or thermocline depth are evident between the two years (2007 and 2018) in either the observations or the simulations (Fig. S2). In the western Getz section—another trough connecting open water to the Getz Ice Shelf—observations show thin mCDW intrusions with a potential temperature of ∼0 °C and a thickness of 50–100 m. By contrast, the simulation produces thicker intrusions (∼200–300 m) that are warmer and more saline (∼1.3 °C, salinity ∼34.66). This discrepancy likely arises from challenges in accurately simulating WW formation and the wind-driven vertical circulation over the continental shelf.

Overall, comparison of vertical sections toward the Pine Island Ice Shelf, the Dotson Ice Shelf, and the Getz Ice Shelf shows that the model is in qualitative agreement with observations. The simulations reproduce key features, including (a) the westward thickening of WW and (b) the coldest mCDW intrusions occurring along the Dotson Trough. However, simulated mCDW properties exhibit biases in several locations, particularly toward the west, where temperatures are warmer than observed by approximately 0.1–0.3 °C (excluding the Siple Trough in March 2007; Table 2) and simulated thermocline depths are shallower. This discrepancy likely reflects challenges in simulating thick WW layers, a common limitation in regional Antarctic continental shelf simulations (Nakayama et al., 2021a).

Mooring observations

We also compare simulated temporal variability with mooring observations (Figs. 9-10). The main feature captured by a compilation of mooring records is a cooling event of 2012–2014, as described by (Dutrieux et al., 2014; Webber et al., 2017; Park et al., 2024), followed by a rebound and weaker cooling event in 2015-16. The larger cooling signals are consistent across the shelf, and observed in the Mid-shelf, PIG-north, and PIG-south moorings. At the PITW mooring, we also detect a slight deepening of the thermocline at a rate of ∼50 m yr^{-1} between January 2013 and January 2014 (defined by the 1.0 °C isotherm depth). In contrast, the eastern-trough mooring (although limited in duration) does not show a comparable cooling.

Overall, the model captures the qualitative pattern of interannual thermocline variability, though several differences emerge. In our simulations, the larger cooling event is reproduced at the Mid-shelf, PIG-north, and PIG-south virtual moorings (based on monthly mean output), but it occurs with an approximately one-year delay relative to observations. In contrast, the phase of

https://doi.org/10.5194/egusphere-2025-5958
Preprint. Discussion started: 3 February 2026

the weaker, follow-on cooling in 2015-16 is captured by the simulation. The simulated PITE and PITW virtual moorings also show a modest thermocline deepening around 2015 of roughly 100 m. Because mooring records at these sites end before 2016, it is difficult to assess whether this simulated deepening is realistic. A persistent warm bias in simulated mCDW temperatures is also evident, consistent with the vertical sections (Fig. 6). When extended over the full simulation period (Fig. S3), the model indicates additional cold phases (i.e., deep thermoclines) in 1995, 1997, 2000, and 2004—periods not covered by observations, as presented in Park et al. (2024).

3.2.2 Bellingshausen Sea

In the Bellingshausen Sea, observations are limited to a few years. Hyogo et al. (2024) conducted a detailed comparison using observations from 2007. Here, we extend this evaluation by comparing our model output with observations from 2019 (Thompson et al., 2020), focusing on sections where repeated measurements are available. No mooring observations have been conducted in the Bellingshausen Sea.

Similar to the Amundsen Sea, both observations and simulations show a consistent hydrographic structure, with cold and fresh WW in the upper layer and mCDW in the lower layer for both 2007 and 2019 at the shelf break of the Belgica trough (Figs. 8 and S4). For the vertical section at the shelf break of the Belgica trough, observations indicate that the thermocline and halocline deepened by ∼100 m between 2007 and 2019. The model reproduces this behavior, showing a similar deepening of ∼100 m (Figs. 8 and S5). In the Belgica and Latady troughs, both observations and simulations show little change in thermocline depth between 2007 and 2019, while the halocline deepened by ∼100 m in the observations and by ∼100 m in the model. Although such changes are influenced by both seasonal and interannual variability, our evaluation suggests that the model skillfully captures the hydrographic structure of the Bellingshausen Sea. A more detailed discussion of circulation and hydrographic variability in this region can be found in Hyogo et al. (2024). Despite the good model data agreement for the thermocline depths, simulated mCDW properties are biased warm and saline by approximately +0.2°C and -0.02, respectively (Table 3).

3.3 Ice-Shelf melting

We compare simulated ice-shelf melt rates with satellite-based estimates (Fig. 11 and Tables 4-5). As shown in previous studies (Hyogo et al., 2024; Park et al., 2024), the model achieves good overall agreement with observations with several regional differences. In the Amundsen Sea, the simulated melt rate of the Cosgrove Ice Shelf is generally higher than observed, whereas the simulated melt rate for the Thwaites Ice Shelf is lower. For the Pine Island, Crosson, Dotson, and Getz ice shelves, agreement with satellite-based estimates varies across different time periods. In the Bellingshausen Sea, the simulated melt rate of the George VI Ice Shelf tends to be higher than satellite-based estimates, and the Wilkins Ice Shelf also exhibits elevated melt rates during 2003–2008 (Rignot et al., 2013). We note that, because we adjust the ice–ocean heat and salt transfer coefficients, it is relatively easy to match the total integrated melt rates for the entire Amundsen or Bellingshausen sectors. However, reproducing realistic regional differences requires accurate simulation of the underlying hydrography and circulation.

https://doi.org/10.5194/egusphere-2025-5958
Preprint. Discussion started: 3 February 2026

We compare time series of ice-shelf melt rates for the major ice shelves in the AS and BS. For most ice shelves, melt rates remain relatively stable, fluctuating around their mean values without significant long-term trends (Fig. 11). We identify several episodes of large variability, though it is unclear whether similar variability occurs in reality. The Abbot and Getz ice shelves, in particular, exhibit pronounced interannual fluctuations. For both ice shelves, melt rates increase notably after 2016, with simulated values rising by factors of approximately three and two, respectively.

We also compare time series of simulated ice-shelf melt rates for Pine Island and Dotson Ice Shelves with oceanography-based estimates (Dutrieux et al., 2014; Heywood et al., 2016; Jenkins et al., 2018) shown in Fig. S6. The agreement between the simulated and observation-based melt rates is generally poor not showing similar temporal variabilities, though within the generally large error bar of the observational estimates. Additional work carefully comparing differences between satellite-based and oceanographic estimates of ice-shelf melt rates, as well as the associated uncertainties, would be useful.

4 Applications

4.1 Model analyses

In the following, we summarize published and ongoing studies that use the same and prior versions of model outputs for process studies, interpretation of observations, sensitivity experiments, and as boundary forcing for downscaled simulations.

Nakayama et al. (2018) used the model to diagnose pathways of CDW onto the continental shelf and quantify their influence on ice-shelf basal melting and shelf heat content. Building on this, Hyogo et al. (2024) examined interannual variability in shelf circulation and heat transport, linking changes to large-scale atmospheric forcing and regional ocean dynamics. Park et al. (2024) further quantified the drivers of local thermocline depth and hydrographic conditions at the Pine Island Ice Shelf front, and explored connections between local circulation and the ocean bottom.

Sensitivity experiments have also been carried out with this model configuration. For example, O'Connor et al. (2025) performed perturbation experiments by repeating selected years of atmospheric forcing to amplify their impact on ocean circulation and hydrography, thereby identifying drivers of interannual variability of the undercurrent. Nakayama et al. (2018) conducted multi-year perturbation experiments by swapping boundary conditions and atmospheric forcing, demonstrating the importance of large-scale ocean circulation in shaping Amundsen Sea hydrography and the properties of CDW intruding onto the West Antarctic continental shelf.

The model output has also been used to provide boundary and initial conditions for higher-resolution nested simulations (Nakayama et al., 2019). These downscaled simulations have been employed to investigate the role of horizontal grid spacing in resolving ocean dynamics across different spatio-temporal scales (Poinelli et al., 2025b). Finally, such simulations have been used to examine submesoscale processes near West Antarctic glaciers and their impacts on modulating submarine ice-shelf melting (Shrestha et al., 2024; Poinelli et al., 2025a), as well as the influence of subglacial freshwater discharge (Nakayama et al., 2021b).

https://doi.org/10.5194/egusphere-2025-5958
Preprint. Discussion started: 3 February 2026

4.2 Sensitivity simulations

We conduct two additional sensitivity simulations to provide a better framework for users. We conduct high-melt and low-melt runs between 2018 and 2023, where we multiply ice-ocean heat and salt transfer coefficients of Pine Island and Thwaites ice shelves by 2 and 0.5, respectively. Simulated melt rate of both ice shelves decreases by 43% (respectively increases by 37%) for the low-melt (respectively high-melt) experiment compared to the control experiment (Table 6).

Because the experiments are conducted for only five years, the impact of the imposed ice-shelf melt anomalies on the ocean is relatively small but still detectable (Figs. 12 and 13). At 250 m depth, which roughly corresponds to the depth of glacial meltwater leaving the ice-shelf cavities, the salinity difference becomes large between these two sensitivity experiments (Fig. 13). The high-melt experiment leads to a slight freshening of 0.02 on the Amundsen continental shelf, while the low-melt experiment leads to a slight increase in salinity of 0.025. Changes in potential temperature are more difficult to discern from the spatial patterns (Fig. 12) and are much smaller than the salinity change. We can still detect a slight broad cooling pattern (Fig. 12a). For depths between 500 and 700 m, which matches the depth of mCDW, the changes are small (Figs. 12b,d), but the pattern is much stable with smaller spatial variability, making it easier to discern the impact of enhanced/reduced melting. By looking at the difference, we observe warmer and saltier mCDW intrusions in the high-melt experiment, likely induced by enhanced ice-shelf melting.

4.3 Passive tracers

The surface restoring tracer in MITgcm can help reveal the fluxes as well as the pathways for ventilation and surface renewal (Fig. 14). Diagnostic variables that describe the tracer transport include both vertical and horizontal advective and diffusive fluxes. Outputs with surface tracer over the past 3 decades have revealed how the isolated mesoscale regions where heat fluxes and ice production are high can effectively reset the entire water column properties above the CDW layer (Fig. 14). These surface restoring tracer simulations provide quantitative insights to the seasonal production of winter water as well as to the restoration of oxygen, and the downward mixing of other surface processes including sea ice and glacial melt. As exemplified by the tracer profiles in the Amundsen Sea Polynya, the model suggests that stratification and surface forcing during multi-year periods can lead to complete penetration into the deepest retrograde troughs, below 1000 m, that lie close to the ice sheet northern terminus. The vertical mixing scheme relies upon the K-Profile Parameterization (KPP) closure model and reveals that turbulent diffusivity dominates the vertical flux of surface tracer within the top 50 m in the region that might typically describe the summer mixed layer. Below 100 m, vertical advective fluxes are the most important ventilation mechanism. In the Belgica Trough of the Bellingshausen Sea, we can also see similar behavior but shallower convection occurs compared to the polynya in the Amundsen Sea (Fig. 14).

The CDW tracer is used to track pathways of mCDW intrusions onto the continental shelf (Figs. 15a,b and Supplementary Movie 2). These intrusions enter from the continental shelf break, following glacially carved troughs, and the pathways become apparent within a few months in both the Amundsen and Bellingshausen Seas (Fig. 15). After three years, a larger amount of CDW occupies the continental shelves. Because the CDW tracer is implemented only as an initial condition, it progressively

https://doi.org/10.5194/egusphere-2025-5958
Preprint. Discussion started: 3 February 2026

mixes as mCDW interacts with and dilutes into glacial meltwater. In the model output, we provide CDW tracer fields only for the first five years; users who wish to examine mCDW intrusions for other periods will need to rerun the tracer experiment.

The ice-shelf melt tracer is used to track the distribution and pathways of meltwater released from ice shelves (Figs. 15c,d and Supplementary Movie 2). The vertically integrated meltwater content shows strong accumulation along the coastline in the first year, followed by increased spreading over the continental shelves within three years. Almost no meltwater is exported to the open ocean because the circulation on the shelf is largely confined, and the potential vorticity (PV) gradient between on-shelf and off-shelf regions inhibits water-mass exchange. This tracer experiment is run continuously throughout the full simulation (1992–2025), but users may restart the experiment from any year if they wish to investigate changes in meltwater pathways. For this purpose, Lagrangian particles can also be used to study meltwater behavior (e.g., Hyogo et al. (2024)).

4.4 Lagrangian Particle Tracking

To complement the Eulerian circulation patterns and passive-tracer diagnostics presented in Sections 4.2 and 4.3, we use forward and backward Lagrangian particle tracking to examine the pathways of mCDW intrusions and the dispersion of meltwater across the Amundsen Sea continental shelf. This analysis reveals how water parcels move through key troughs, reach the ice-shelf cavities, and interact with coastal currents.

Hydrographic sections (Fig. 7) indicate that the Siple Trough hosts a relatively warm and persistent mCDW intrusion, with a deep thermocline and a two-layer structure. Based on this structure, particles were released off the shelf break at 600–750 m, consistent with the depth of the mCDW core in observations and simulations (Fig. 16). The resulting trajectories (Fig. 17 and Supplementary Movie 3) show that offshore parcels cross the shelf break near 73.1°S and follow the eastern flank of the trough toward the Getz Ice Shelf front. Near Din Island, particles enter a cyclonic flow that redistributes them along the 700 m isobath before either recirculating near the ice front or moving westward along the slope.

We also provide examples of how ice-shelf meltwater travels in time from the Dotson, Pine Island, and Thwaites ice shelves (Fig. 18 and Supplementary Movies 4-6). In the forward experiments, particles released just seaward of each ice-shelf front show that meltwater is rapidly entrained into the westward Antarctic Coastal Current and advected along the coast. This behavior is consistent with previous studies documenting coastal pathways of meltwater export.

To determine the origin of the warm water entering the ice-shelf cavities, we conduct backward particle-tracking experiments. Particles released below 700 m in the deep Dotson and Pine Island Bay troughs were tracked backward for 12 months (Fig. 19 and Supplementary Movies 7-8). The resulting pathways show that mCDW supplying Dotson arrives mainly through the western trough, while mCDW feeding Pine Island and Thwaites enters via the central and eastern troughs, underscoring the strong topographic control on warm-water access.

The forward and backward particle-tracking experiments provide a coherent Lagrangian view of how warm mCDW and meltwater circulate within the Amundsen Sea. They strengthen the interpretation of the Eulerian and tracer-based analyses and highlight key pathways where targeted observations would be most effective.

https://doi.org/10.5194/egusphere-2025-5958
Preprint. Discussion started: 3 February 2026

5 Conclusions

In this study, we assess the performance of the ECCO-LLC270 downscaled model for the Amundsen and Bellingshausen Seas, focusing on sea ice, ocean, and ice-shelf melting. The model reproduces key characteristics of regional sea-ice variability, captures the main ocean circulation features and water-mass distributions, and simulates ice-shelf basal melt rates that align with observations. Beyond these core evaluations, we demonstrate how passive tracers, Lagrangian particles, and sensitivity experiments can be used to investigate water-mass pathways, meltwater dispersal, and the physical mechanisms driving ocean–ice interactions. Importantly, the model configuration, code, and outputs are shared to be user-friendly and accessible, allowing researchers from diverse backgrounds — including those outside traditional ocean modeling — to explore, interpret, and build upon the simulations. By providing a common, well-evaluated "control" experiment, this work facilitates intercomparison studies, supports hypothesis testing, and encourages broader, multidisciplinary investigations of the rapidly changing Southern Ocean.

Code and data availability. The current version of MITgcm is available from the project website https://mitgcm.readthedocs.io/en/latest/ under MIT license. The exact version of the model used to produce the results used in this paper is 66j archived on repository under https://github.com/MITgcm/MITgcm. Model code, input, and output are available from https://ecco.jpl.nasa.gov/drive/files/ECCO2/LLC1080_REG_AMS/Nakayama_in_prep (last access: 1 December 2025). Model code and input are available also from https://doi.org/10.5281/zenodo.18446202 (Nakayama, 2025). All scripts are provided upon request during the first revision, and all code, output, and scripts will all be deposited on Zenodo prior to the second revision.

Author contributions. Y.N. conceived the study. S.H., Y.L., T.P., J.L., G.M., M.P., P.D., K.N., B.L., L.K., and J.C. conducted model/observation analyses for comparison. H.Z. developed the extension of ECCO-LLC270 simulations up to 2025. All authors discussed the results and implications and commented on the manuscript at all stages.

Competing interests. The authors declare no competing interests.

6 Acknowledgments

YN was supported by the funds from NASA Sea Level Change Team (80NSSC24K1532), JST PRESTO, Japan (Grant Number JPMJPR25G5), and Grants-in-Aid for Scientific Research of the Japanese Ministry of Education, Culture, Sports, Science and Technology (24H02341). TP was supported by the Korea Institute of Marine Science and Technology Promotion (KIMST) under funding from the Korean Ministry of Oceans and Fisheries (Grant No. RS-2023-00256677; PM24020) and additional support for TP and JL was provided by the Korea Polar Research Institute (Grant No. PE24110). MP was supported by the

https://doi.org/10.5194/egusphere-2025-5958
Preprint. Discussion started: 3 February 2026

NASA Cryospheric Sciences Program (Grant No. 80NM0018F0585). JC is supported by the NASA Sea Level Change Team Program (Grants No. 80NSSC24K1532 and 80NSSC21K0322). Some of the figures are produced with Ocean Data View Schlitzer (2004).

https://doi.org/10.5194/egusphere-2025-5958
Preprint. Discussion started: 3 February 2026

References

Antonov, J. I., Seidov, D., Boyer, T. P., Locarnini, R. A., Mishonov, A. V., Garcia, H. E., Baranova, O. K., Zweng, M. M., and Johnson, D. R.: World Ocean Atlas 2009, Volume 2: Salinity, S. Levitus, Ed., NOAA Atlas NESDIS 69, U.S. Government Printing Office, Washington, D.C., 2010.

Arndt, J. E., Schenke, H. W., Jakobsson, M., Nitsche, F. O., Buys, G., Goleby, B., Rebesco, M., Bohoyo, F., Hong, J., Black, J., et al.: The International Bathymetric Chart of the Southern Ocean (IBCSO) Version 1.0 A new bathymetric compilation covering circum-Antarctic waters, Geophysical Research Letters, 40, 3111–3117, 2013.

Assmann, K., Jenkins, A., Shoosmith, D., Walker, D., Jacobs, S., and Nicholls, K.: Variability of circumpolar deep water transport onto the Amundsen Sea continental shelf through a shelf break trough, Journal of Geophysical Research, 118, 6603–6620, 2013.

Assmann, K., Darelius, E., Wåhlin, A. K., Kim, T.-W., and Lee, S. H.: Warm Circumpolar Deep Water at the Western Getz Ice Shelf Front, Antarctica, Geophysical Research Letters, 46, 870–878, 2019.

Bett, D. T., Holland, P. R., Naveira Garabato, A. C., Jenkins, A., Dutrieux, P., Kimura, S., and Fleming, A.: The impact of the Amundsen Sea freshwater balance on ocean melting of the West Antarctic Ice Sheet, Journal of Geophysical Research: Oceans, 125, e2020JC016 305, 2020.

Caillet, J., Jourdain, N. C., Mathiot, P., Hellmer, H. H., and Mouginot, J.: Drivers and Reversibility of Abrupt Ocean State Transitions in the Amundsen Sea, Antarctica, Journal of Geophysical Research: Oceans, 128, e2022JC018 929, https://doi.org/10.1029/2022JC018929, 2023.

Castro-Morales, K., Cassar, N., Shoosmith, D. R., and Kaiser, J.: Biological production in the Bellingshausen Sea from oxygen-to-argon ratios and oxygen triple isotopes, Biogeosciences, 10, 2273–2291, 2013.

Comiso, J.: Bootstrap Sea Ice Concentrations from Nimbus-7 SMMR and DMSP SSM/I-SSMIS, Version 4, https://doi.org/10.5067/X5LG68MH013O, 2023.

De Rydt, J., Holland, P., Dutrieux, P., and Jenkins, A.: Geometric and oceanographic controls on melting beneath Pine Island Glacier, Journal of Geophysical Research: Oceans, 119, 2420–2438, 2014.

Dee, D., Uppala, S., Simmons, A., Berrisford, P., Poli, P., Kobayashi, S., Andrae, U., Balmaseda, M., Balsamo, G., Bauer, P., et al.: The ERA-Interim reanalysis: Configuration and performance of the data assimilation system, Quarterly Journal of the Royal Meteorological Society, 137, 553–597, 2011.

Depoorter, M., Bamber, J., Griggs, J., Lenaerts, J., Ligtenberg, S., van den Broeke, M., and Moholdt, G.: Calving fluxes and basal melt rates of Antarctic ice shelves, Nature, 502, 89–92, 2013.

Donat-Magnin, M., Jourdain, N. C., Kittel, C., Agosta, C., Amory, C., Gallée, H., Krinner, G., and Chekki, M.: Future surface mass balance and surface melt in the Amundsen sector of the West Antarctic Ice Sheet, The Cryosphere, 15, 571–593, 2021.

Dutrieux, P., De Rydt, J., Jenkins, A., Holland, P. R., Ha, H. K., Lee, S. H., Steig, E. J., Ding, Q., Abrahamsen, E. P., and Schröder, M.: Strong sensitivity of Pine Island ice-shelf melting to climatic variability, Science, 343, 174–178, 2014.

Forget, G., Campin, J.-M., Heimbach, P., Hill, C. N., Ponte, R. M., and Wunsch, C.: ECCO version 4: An integrated framework for non-linear inverse modeling and global ocean state estimation, 2015.

Fraser, A. D., Massom, R. A., Ohshima, K. I., Willmes, S., Kappes, P. J., Cartwright, J., and Porter-Smith, R.: High-resolution mapping of circum-Antarctic landfast sea ice distribution, 2000–2018, Earth System Science Data, 12, 2987–2999, https://doi.org/10.5194/essd-12-2987-2020, 2020.

https://doi.org/10.5194/egusphere-2025-5958
Preprint. Discussion started: 3 February 2026

Hellmer, H. and Olbers, D.: A two-dimensional model for the thermohaline circulation under an ice shelf, Antarctic Science, 1, 325–336, 1989.

Heywood, K. J., Biddle, L. C., Boehme, L., Dutrieux, P., Fedak, M., Jenkins, A., Jones, R. W., Kaiser, J., Mallett, H., Garabato, A. C. N., et al.: Between the devil and the deep blue sea: the role of the Amundsen Sea continental shelf in exchanges between ocean and ice shelves, Oceanography, 29, 118–129, 2016.

Holland, D. M. and Jenkins, A.: Modeling thermodynamic ice-ocean interactions at the base of an ice shelf, J. Phys. Oceanogr., 29, 1787–1800, 1999.

Hyogo, S., Nakayama, Y., and Mensah, V.: Modeling ocean circulation and ice shelf melt in the Bellingshausen Sea, Journal of Geophysical Research: Oceans, 129, e2022JC019 275, 2024.

Jacobs, S., Jenkins, A., Hellmer, H., Giulivi, C., Nitsche, F., Huber, B., and Guerrero, R.: The Amundsen Sea and the Antarctic Ice Sheet, Oceanography, 25, 154–163, 2012.

Jacobs, S. S., Hellmer, H. H., and Jenkins, A.: Antarctic ice sheet melting in the Southeast Pacific, Geophysical Research Letters, 23, 957–960, 1996.

Jacobs, S. S., Jenkins, A., Giulivi, C. F., and Dutrieux, P.: Stronger ocean circulation and increased melting under Pine Island Glacier ice shelf, Nature Geoscience, 4, 519–523, 2011.

Jenkins, A., Shoosmith, D., Dutrieux, P., Jacobs, S., Kim, T. W., Lee, S. H., Ha, H. K., and Stammerjohn, S.: West Antarctic Ice Sheet retreat in the Amundsen Sea driven by decadal oceanic variability, Nature Geoscience, 11, 733–738, 2018.

Jourdain, N. C., Mathiot, P., Merino, N., Durand, G., Le Sommer, J., Spence, P., Dutrieux, P., and Madec, G.: Ocean circulation and sea-ice thinning induced by melting ice shelves in the Amundsen Sea, Journal of Geophysical Research: Oceans, 122, 2550–2573, 2017.

Jourdain, N. C., Mathiot, P., Burgard, C., Caillet, J., and Kittel, C.: Ice shelf basal melt rates in the Amundsen Sea at the end of the 21st century, Geophysical Research Letters, 49, e2022GL100 629, 2022.

Kaleschke, L., Tian-Kunze, X., Hendricks, S., and Ricker, R.: SMOS-derived Antarctic thin sea ice thickness: data description and validation in the Weddell Sea, Earth System Science Data, 16, 3149–3170, https://doi.org/10.5194/essd-16-3149-2024, 2024.

Kim, I., Hahm, D., Rhee, T. S., Kim, T. W., Kim, C.-S., and Lee, S.: The distribution of glacial meltwater in the Amundsen Sea, Antarctica, revealed by dissolved helium and neon, Journal of Geophysical Research: Oceans, 2016.

Kim, T.-W., Ha, H. K., Wåhlin, A., Lee, S., Kim, C.-S., Lee, J. H., and Cho, Y.-K.: Is Ekman pumping responsible for the seasonal variation of warm circumpolar deep water in the Amundsen Sea?, Continental Shelf Research, 132, 38–48, 2017.

Kimura, S., Jenkins, A., Regan, H., Holland, P. R., Assmann, K. M., Whitt, D. B., Van Wessem, M., van de Berg, W. J., Reijmer, C. H., and Dutrieux, P.: Oceanographic controls on the variability of ice-shelf basal melting and circulation of glacial meltwater in the Amundsen Sea Embayment, Antarctica, Journal of Geophysical Research: Oceans, 122, 10 131–10 155, 2017.

Lin, Y., Nakayama, Y., Liang, K., Huang, Y., Chen, D., and Yang, Q.: Daily Edge of Each Polynya in Antarctic (DEEP-AA), https://doi.org/10.5281/zenodo.13358042, 2024a.

Lin, Y., Nakayama, Y., Liang, K., Huang, Y., Chen, D., and Yang, Q.: A dataset of the daily edge of each polynya in the Antarctic, Scientific Data, 11, 1006, 2024b.

Locarnini, R. A., Mishonov, A. V., Antonov, J. I., Boyer, T. P., and Garcia, H. E.: World Ocean Atlas 2009, Volume 1: Temperature, S. Levitus, Ed., NOAA Atlas NESDIS 68, U.S. Government Printing Office, Washington, D.C., 2010.

Losch, M.: Modeling ice shelf cavities in a z coordinate ocean general circulation model, Journal of Geophysical Research: Oceans, 113, 2008.

https://doi.org/10.5194/egusphere-2025-5958
Preprint. Discussion started: 3 February 2026

Losch, M., Menemenlis, D., Heimbach, P., Campin, J.-M., and Hill, C.: On the formulation of sea-ice models. Part 1: Effects of different solver implementations and parameterizations, Ocean Model., 33, 129–144, 2010.

Morlighem, M.: MEaSUREs BedMachine Antarctica, Version 3, https://doi.org/10.5067/FPSU0V1MWUB6, 2022.

Nakata, K. and Ohshima, K. I.: Mapping of Active Frazil and Sea Ice Production in the Northern Hemisphere, With Comparison to the Southern Hemisphere, Journal of Geophysical Research: Oceans, 127, e2022JC018 553, https://doi.org/https://doi.org/10.1029/2022JC018553, 2022.

Nakayama, Y.: MITgcm model code and input for "Development of ECCO-downscaled Amundsen-Bellingshausen Sea regional simulation using MITgcm(66j)", Zenodo, https://doi.org/10.5281/zenodo.18446202, 2025.

Nakayama, Y., Schröder, M., and Hellmer, H. H.: From circumpolar deep water to the glacial meltwater plume on the eastern Amundsen Shelf, Deep Sea Research Part I: Oceanographic Research Papers, 77, 50–62, 2013.

Nakayama, Y., Timmermann, R., Rodehacke, C. B., Schröder, M., and Hellmer, H. H.: Modeling the spreading of glacial meltwater from the Amundsen and Bellingshausen Seas, Geophysical Research Letters, 41, 7942–7949, 2014a.

Nakayama, Y., Timmermann, R., Schröder, M., and Hellmer, H.: On the difficulty of modeling Circumpolar Deep Water intrusions onto the Amundsen Sea continental shelf, Ocean Modelling, 84, 26–34, 2014b.

Nakayama, Y., Menemenlis, D., Schodlok, M., and Rignot, E.: Amundsen and B ellingshausen S eas simulation with optimized ocean, sea ice, and thermodynamic ice shelf model parameters, Journal of Geophysical Research: Oceans, 122, 6180–6195, 2017.

Nakayama, Y., Menemenlis, D., Zhang, H., Schodlok, M., and Rignot, E.: Origin of Circumpolar Deep Water intruding onto the Amundsen and Bellingshausen Sea continental shelves, Nature communications, 9, 1–9, 2018.

Nakayama, Y., Manucharayan, G., Kelin, P., Torres, H. G., Schodlok, M., Rignot, E., Dutrieux, P., and Menemenlis, D.: Pathway of Circumpolar Deep Water into Pine Island and Thwaites ice shelf cavities and to their grounding lines, Scientific Reports, 2019.

Nakayama, Y., Greene, C. A., Paolo, F. S., Mensah, V., Zhang, H., Kashiwase, H., Simizu, D., Greenbaum, J. S., Blankenship, D. D., Abe-Ouchi, A., et al.: Antarctic slope current modulates ocean heat intrusions towards Totten glacier, Geophysical Research Letters, 48, e2021GL094 149, 2021a.

Nakayama, Y., Menemenlis, D., Wang, O., Zhang, H., Fenty, I., and Nguyen, A. T.: Development of adjoint-based ocean state estimation for the Amundsen and Bellingshausen seas and ice shelf cavities using MITgcm–ECCO (66j), Geoscientific Model Development, 14, 4909–4924, 2021b.

Naughten, K. A., Holland, P. R., Dutrieux, P., Kimura, S., Bett, D. T., and Jenkins, A.: Simulated Twentieth-Century Ocean Warming in the Amundsen Sea, West Antarctica, Geophysical Research Letters, 49, e2021GL094 566, 2022.

Naughten, K. A., Holland, P. R., and De Rydt, J.: Unavoidable future increase in West Antarctic ice-shelf melting over the twenty-first century, Nature Climate Change, 13, 1222–1228, 2023.

Ohshima, K. I., Nihashi, S., and Iwamoto, K.: Global view of sea-ice production in polynyas and its linkage to dense/bottom water formation, Geoscience Letters, 3, 13, https://doi.org/10.1186/s40562-016-0045-4, 2016.

O'Connor, G. K., Nakayama, Y., Steig, E. J., Armour, K. C., Thompson, L., Hyogo, S., Berdahl, M., and Shimada, T.: Enhanced West Antarctic ice loss triggered by polynya response to meridional winds, Nature Geoscience, 18, 840–847, 2025.

Paolo, F. S., Fricker, H. A., and Padman, L.: Volume loss from Antarctic ice shelves is accelerating, Science, 348, 327–331, 2015.

Park, T., Nakayama, Y., and Nam, S.: Amundsen Sea circulation controls bottom upwelling and Antarctic Pine Island and Thwaites ice shelf melting, Nature Communications, 15, 2946, 2024.

https://doi.org/10.5194/egusphere-2025-5958
Preprint. Discussion started: 3 February 2026

Poinelli, M., Siegelman, L., and Nakayama, Y.: Ocean submesoscales as drivers of submarine melting within Antarctic ice cavities, Nature Geoscience, 2025a.

Poinelli, M., Siegelman, L., Nakayama, Y., Rignot, E., Seroussi, H., Fenty, I., and Larour, E.: Small-scale, high-frequency ice, and ocean processes in the Amundsen Sea Embayment, West Antarctica., Journal of Advances in Modeling Earth Systems, 17, 2025b.

Rignot, E., Jacobs, S. S., Mouginot, J., and Scheuchl, B.: Ice-shelf melting around Antarctica, Science Express, 341, 226–270, 2013.

Schlitzer, R.: Ocean data view, Alfred Wegener Institute for Polar and Marine Research: Bermerhaven, Germany, 2004.

Shepherd, A., Ivins, E., Geruo, A., Barletta, V., Bentley, M., Bettadpur, S., Briggs, K., Bromwich, D., Forsberg, R., Galin, N., et al.: A reconciled estimate of ice-sheet mass balance, Science, 338, 1183–1189, 2012.

Shrestha, K., Manucharyan, G. E., and Nakayama, Y.: Submesoscale variability and basal melting in ice shelf cavities of the Amundsen Sea, Geophysical Research Letters, 51, e2023GL107 029, 2024.

St-Laurent, P., Yager, P., Sherrell, R., Stammerjohn, S., and Dinniman, M.: Pathways and supply of dissolved iron in the Amundsen Sea (Antarctica), Journal of Geophysical Research: Oceans, 122, 7135–7162, 2017.

St-Laurent, P., Yager, P., Sherrell, R., Oliver, H., Dinniman, M., and Stammerjohn, S.: Modeling the seasonal cycle of iron and carbon fluxes in the Amundsen Sea Polynya, Antarctica, Journal of Geophysical Research: Oceans, 124, 1544–1565, 2019.

St-Laurent, P., Stammerjohn, S., and Maksym, T.: Response of onshore oceanic heat supply to yearly changes in the Amundsen Sea icescape (Antarctica), Journal of Geophysical Research: Oceans, 129, e2023JC020 467, 2024.

Thoma, M., Jenkins, A., Holland, D., and Jacobs, S.: Modelling circumpolar deep water intrusions on the Amundsen Sea continental shelf, Antarctica, Geophysical Research Letters, 35, 2008.

Thompson, A. F., Speer, K. G., and Schulze Chretien, L. M.: Genesis of the Antarctic Slope Current in West Antarctica, Geophysical Research Letters, 47, e2020GL087 802, 2020.

Tian-Kunze, X. and Kaleschke, L.: SMOS-derived sea ice thickness in the Antarctic from 2010 to 2020, https://doi.org/10.1594/PANGAEA.934732, 2021.

Van Achter, G., Fichefet, T., Goosse, H., Pelletier, C., Sterlin, J., Huot, P.-V., Lemieux, J.-F., Fraser, A. D., Haubner, K., and Porter-Smith, R.: Modelling landfast sea ice and its influence on ocean–ice interactions in the area of the Totten Glacier, East Antarctica, Ocean Modelling, 169, 101 920, 2022.

Webber, B. G., Heywood, K. J., Stevens, D. P., Dutrieux, P., Abrahamsen, E. P., Jenkins, A., Jacobs, S. S., Ha, H. K., Lee, S. H., and Kim, T. W.: Mechanisms driving variability in the ocean forcing of Pine Island Glacier, Nature communications, 8, 1–8, 2017.

Wunsch, C. and Heimbach, P.: Dynamically and kinematically consistent global ocean circulation and ice state estimates, in: International Geophysics, vol. 103, pp. 553–579, Elsevier, 2013.

Zhang, H., Menemenlis, D., and Fenty, I.: ECCO LLC270 Ocean-Ice State Estimate, 2018.

https://doi.org/10.5194/egusphere-2025-5958
Preprint. Discussion started: 3 February 2026

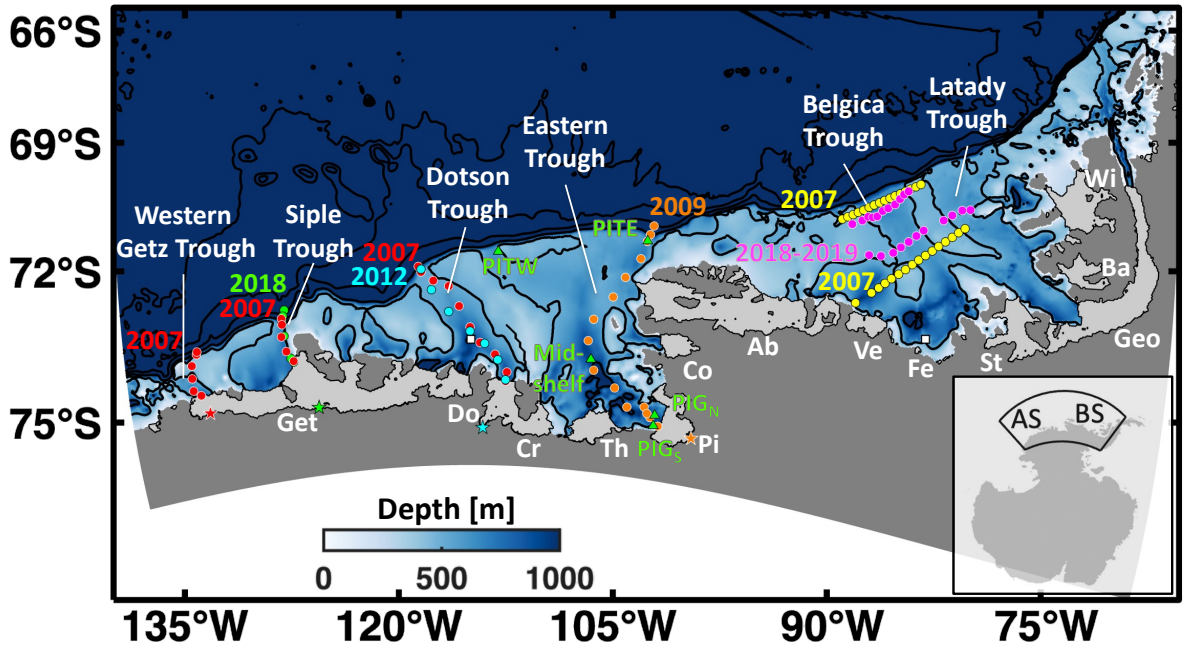

Figure 1. Map of model bathymetry (color). Bathymetric contours of 500, 1000, 2000, 3000, and 4000 m are shown with black contours. The inset (bottom right) shows Antarctica with the region surrounded by a black line denoting the model domain. Locations of hydrographic profiles collected from cruise JR165 (yellow circles), cruise NBP07-02 (red circles), NBP09-01 (orange circles), ANA02C (cyan circles), ANA08B (green circles), and NBP19-01 (magenta circles) are shown. The colored stars indicate the southern endpoints of the model sections—extended beneath the ice shelves—for the Eastern Trough (orange star), Dotson Trough (cyan star), Siple Trough (green star), and Western Getz Trough (red star) (Figures 6–8, S1–S2, and S4–S5). The four-digit numbers near each observation site indicate the year of observation (for the datasets used in this study only). Green triangles indicate the moored stations. The locations of ice shelves are shown with light gray color: Getz Ice Shelf (Get), Dotson Ice Shelf (Do), Crosson Ice Shelf (Cr), Thwaites Ice Shelf (Th), Pine Island Ice Shelf (Pi), Cosgrove Ice Shelf (Co), Abbot Ice Shelf (Ab), George VI Ice Shelf (Geo), Venable Ice Shelf (Ve), Ferrigno Ice Shelf (Fe), Stange Ice Shelf (St), George VI Ice Shelf (Geo), Wilkins Ice Shelf (Wi), and Bach Ice Shelf (Ba). White squares indicate the locations where hovmeller diagrams of surface restoring tracer are shown (Fig. 14).

https://doi.org/10.5194/egusphere-2025-5958
Preprint. Discussion started: 3 February 2026

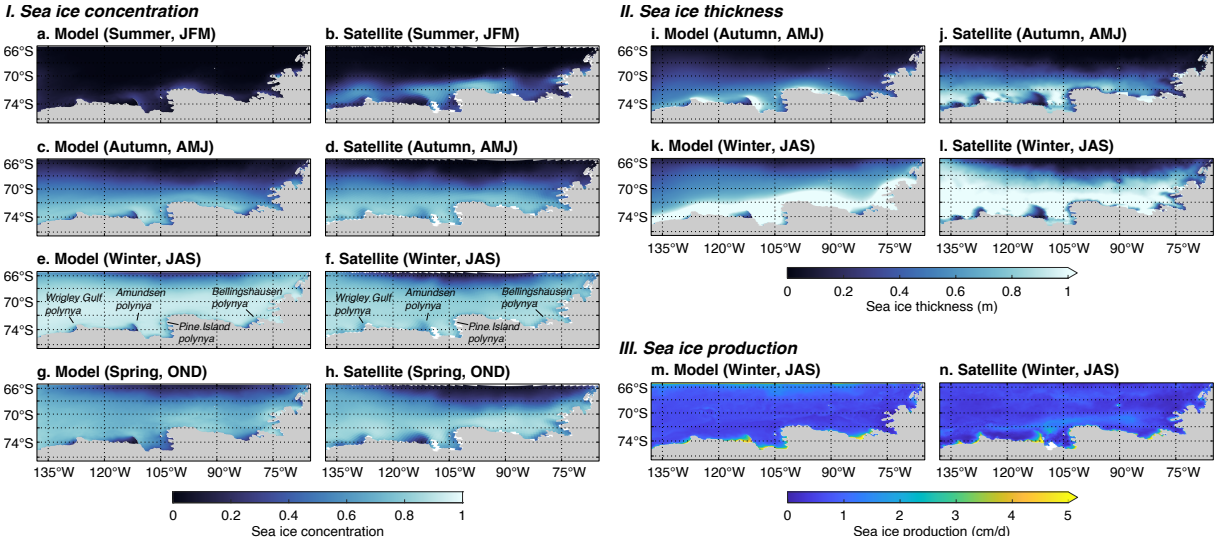

Figure 2. Comparison of sea ice concentration (Group I), thickness (Group II), and production (Group III) with remote sensing data. The left column (a, c, e, g, I, k, m) comes from the model; the right column (b, d, f, h, j, l, n) comes from the remote sensing data. The seasons and the corresponding months for comparison are marked at the top of each subfigure. In (e) and (f), the 4 main polynyas have been marked.

https://doi.org/10.5194/egusphere-2025-5958
Preprint. Discussion started: 3 February 2026

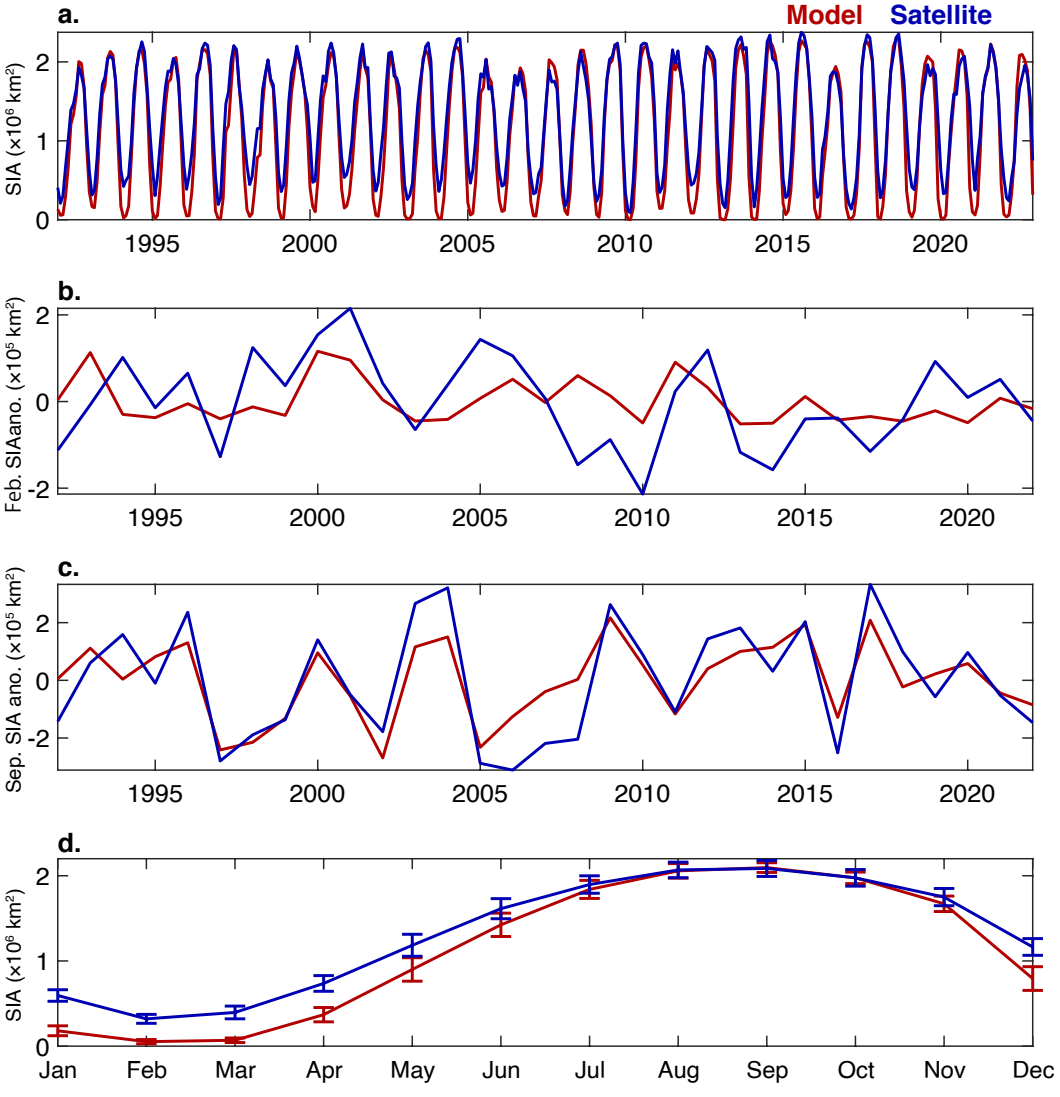

Figure 3. Simulated and satellite-based observed (a) time series of sea ice area (SIA), (b, c) SIA anomalies for February and September, and (d) the climatological SIA seasonal cycle. For (d), error bars represent 1 standard deviation of variability.

https://doi.org/10.5194/egusphere-2025-5958
Preprint. Discussion started: 3 February 2026

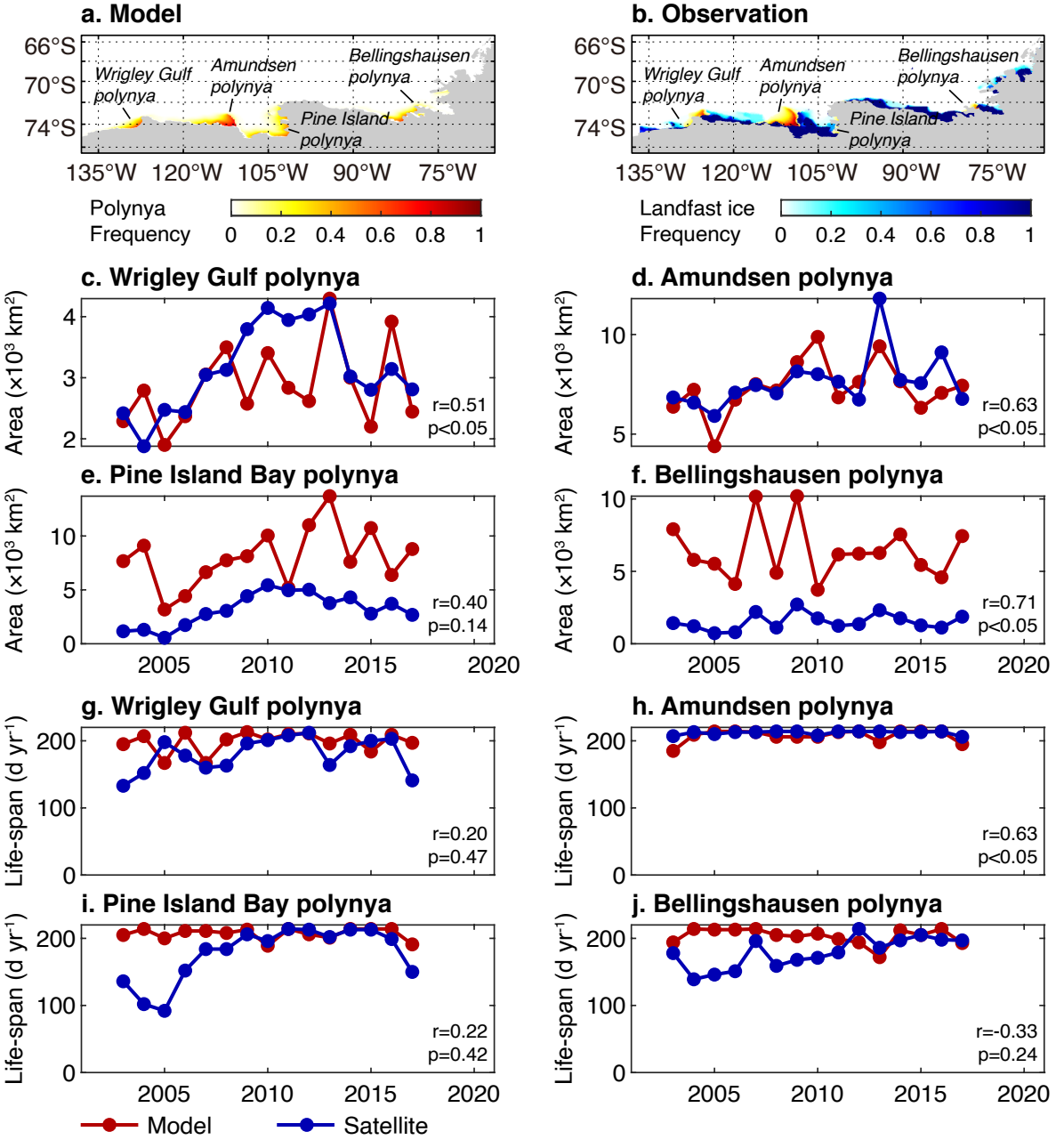

Figure 4. Evaluation of the area and life span of polynyas in the model. (a) and (b) are the frequency maps of polynyas (warm color) and landfast ice (cold color) from the model and observation, respectively. (c)-(f) plots the area; (g)-(j) plots the life-span. The red lines indicate the results from the model, and the blue lines indicate those from remote sensing data. Their correlation coefficient is marked on the figure.

https://doi.org/10.5194/egusphere-2025-5958
Preprint. Discussion started: 3 February 2026

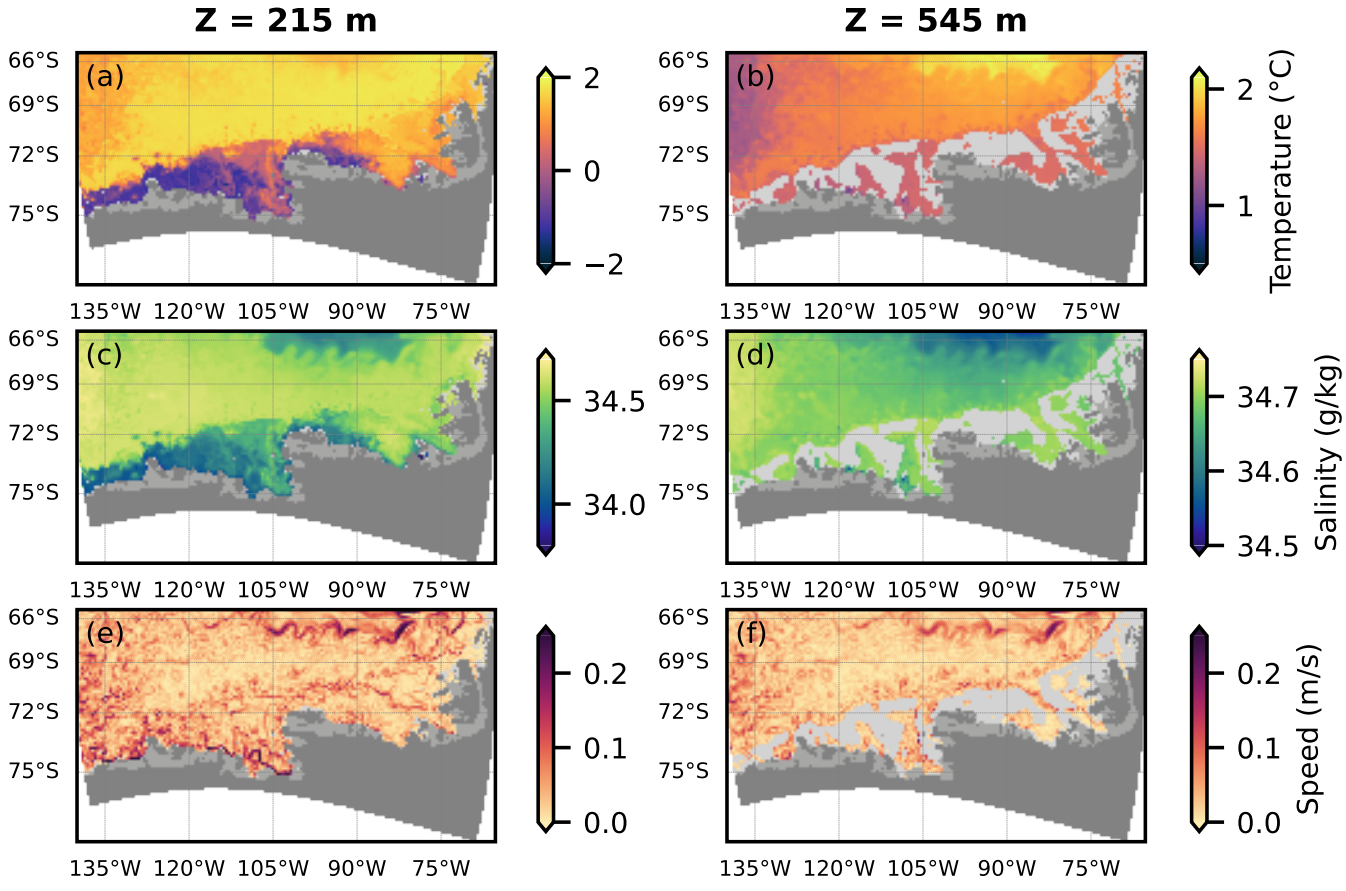

Figure 5. Main characteristics of the ocean in January 2025 at 215 m (left column) and 525 m (right column) depths. (a-b) potential temperature, (c-d) salinity, and (e-f) velocity. The light gray areas represent the areas under bathymetry. The dark gray and gray areas represent the grounded ice sheet and floating ice shelves, respectively.

https://doi.org/10.5194/egusphere-2025-5958
Preprint. Discussion started: 3 February 2026

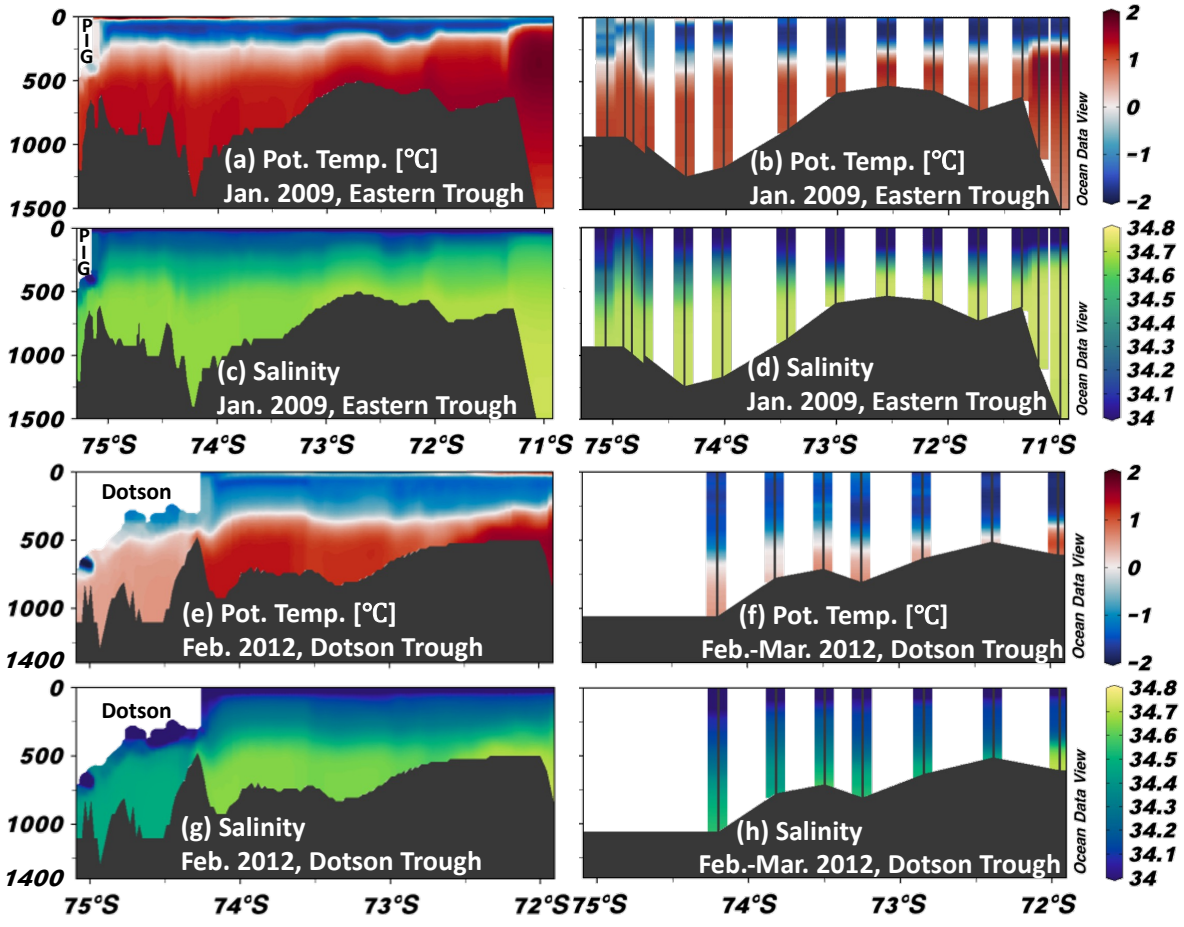

Figure 6. Simulated vertical sections of (a, e) potential temperature and (c, g) salinity along the Eastern Trough (2009) and Dotson (2012) transects, using monthly mean fields for the corresponding observation months. The model sections are extended further south to illustrate the hydrographic structure within the ice-shelf cavities (see the orange and cyan stars in Fig. 1). Observed vertical sections of (b, f) potential temperature and (d, h) salinity along the same transects are also shown.

https://doi.org/10.5194/egusphere-2025-5958
Preprint. Discussion started: 3 February 2026

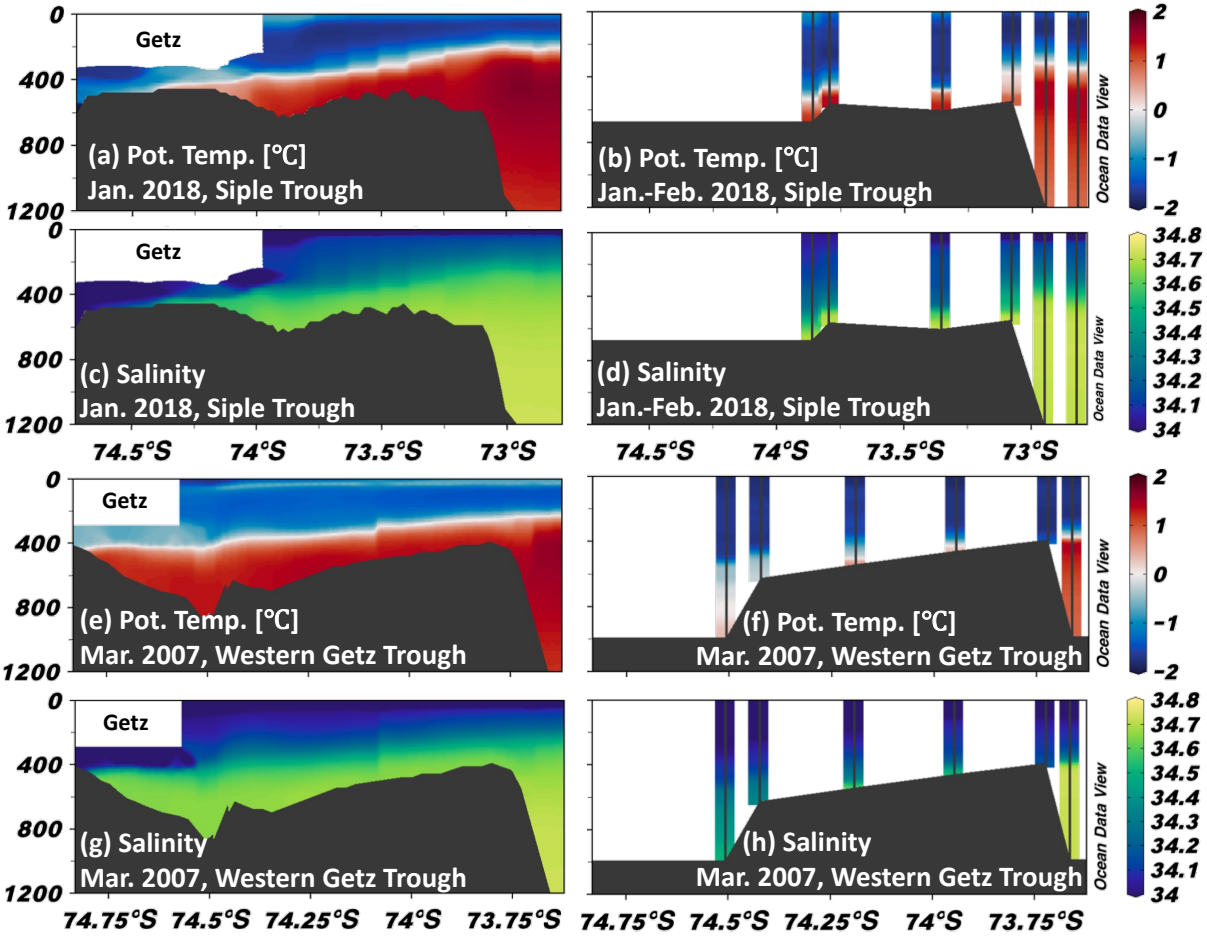

Figure 7. Same as in Fig. 6, but for Siple (2018) and Western Getz troughs (2007). The model sections are extended southward into the ice-shelf cavities (see the green and red stars in Fig. 1). A comparison with the 2007 Siple trough section is shown in Fig. S2.

https://doi.org/10.5194/egusphere-2025-5958
Preprint. Discussion started: 3 February 2026

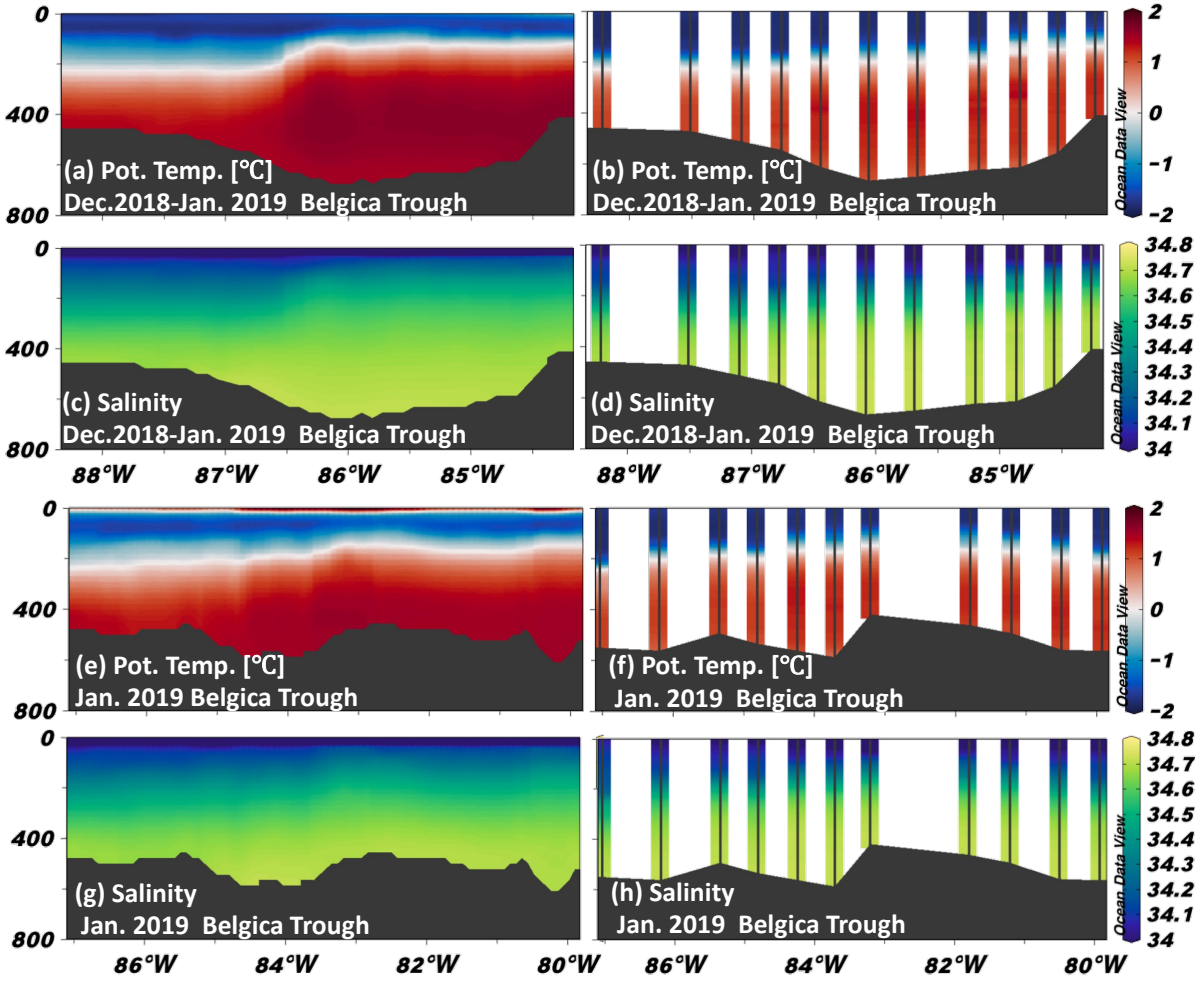

Figure 8. Same as in Fig. 6, but for vertical sections crossing Belgica trough using 2018-2019 observations in BS. A comparison with the 2007 Belgica trough section is shown in Figs. S4 and S5.

https://doi.org/10.5194/egusphere-2025-5958
Preprint. Discussion started: 3 February 2026

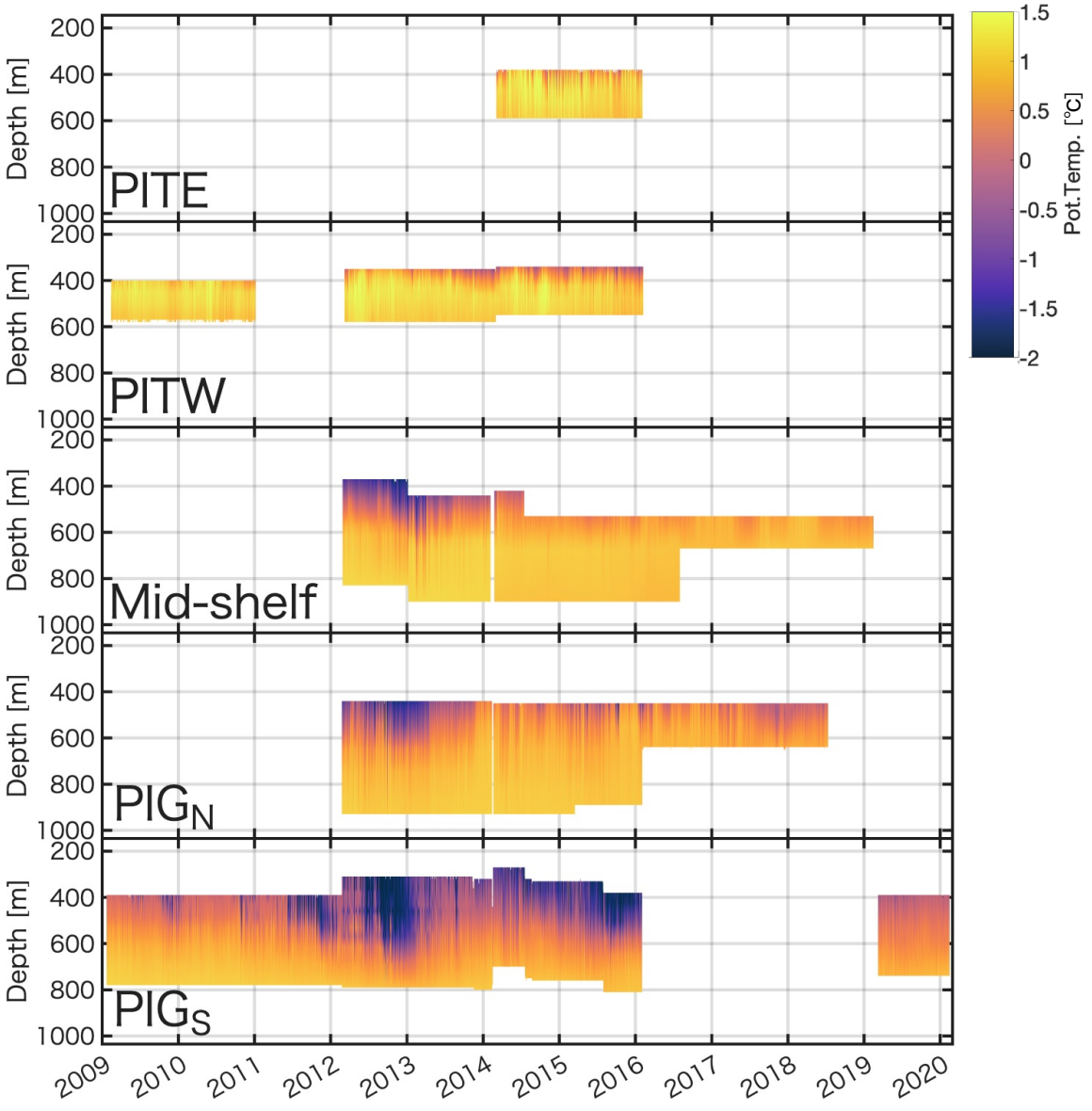

Figure 9. Time series of in situ temperature from mooring data located in the eastern Amundsen Sea. The mooring locations are shown in Figure 1. We present in situ temperature measurements here because salinity data are not available at the same depths as the temperature sensors. The difference between potential temperature and in situ temperature is small—calculated to be less than 0.03°C at a depth of 500 m, assuming a salinity of 34.4.

https://doi.org/10.5194/egusphere-2025-5958
Preprint. Discussion started: 3 February 2026

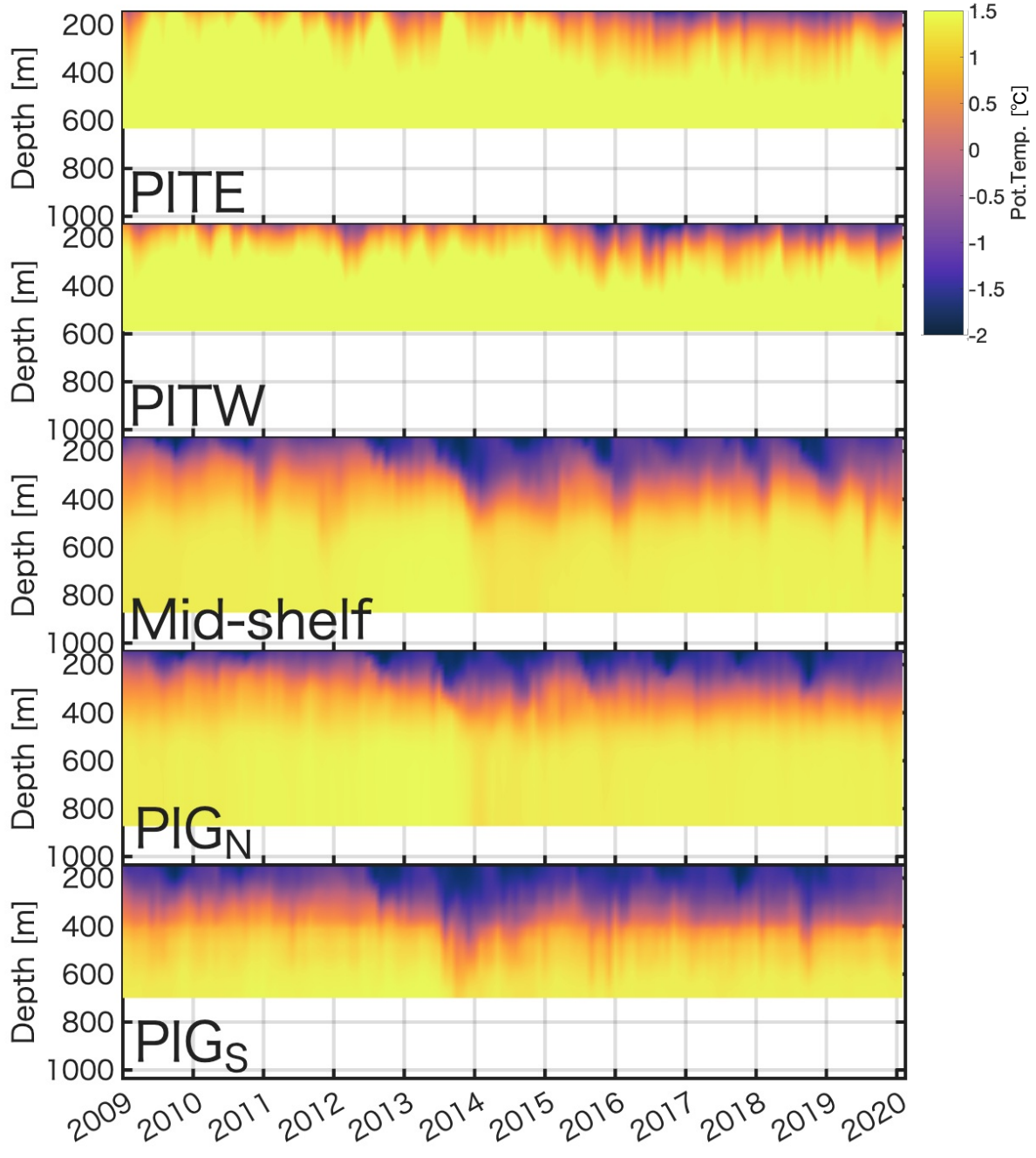

Figure 10. Same as Figure 11, but showing simulated potential temperature from the monthly model output between January 2009 and February 2020.

https://doi.org/10.5194/egusphere-2025-5958
Preprint. Discussion started: 3 February 2026

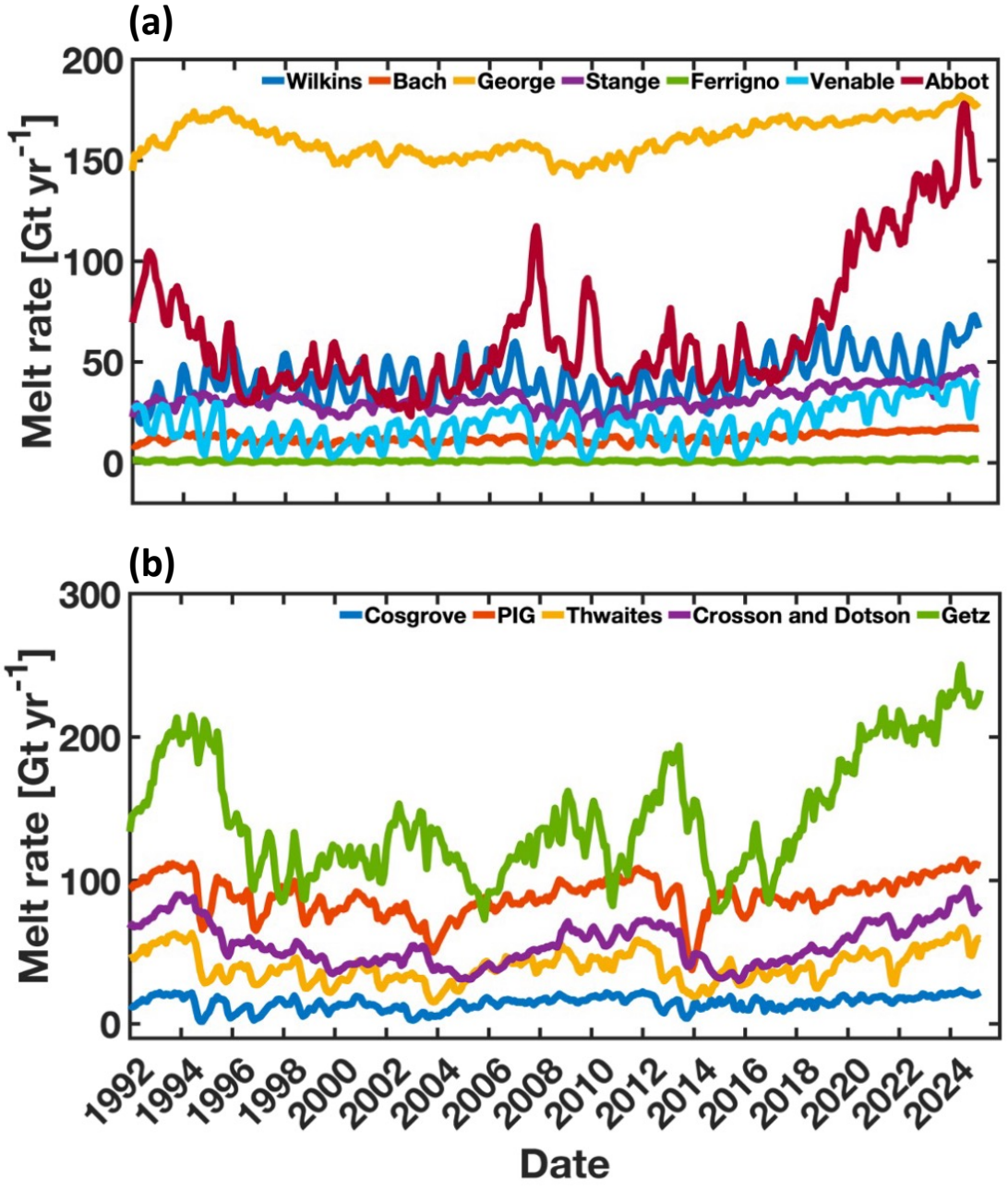

Figure 11. Time series of simulated ice-shelf melt rates in the (a) Bellingshausen Sea (BS) and (b) Amundsen Sea (AS). Each color represents the area-integrated melt rate for an individual ice shelf, as indicated in the legend at the top of each panel.

https://doi.org/10.5194/egusphere-2025-5958
Preprint. Discussion started: 3 February 2026

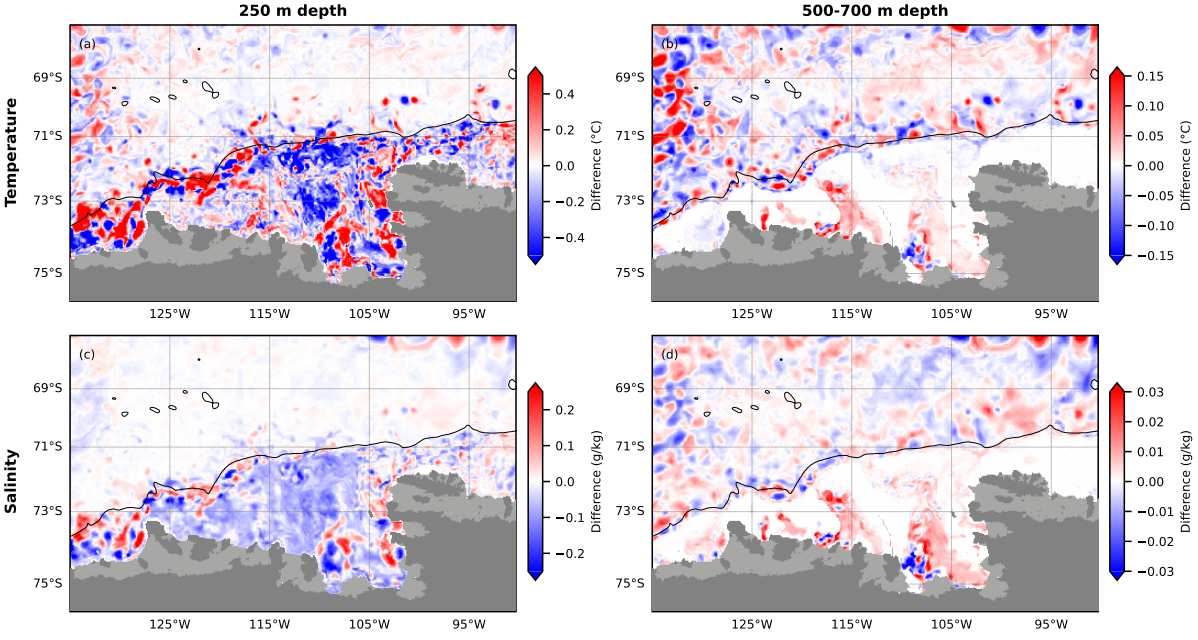

Figure 12. (a,c) Difference in potential temperature and salinity at 250 m depth between high-melt (High) and low-melt (Low) experiments, after 5 years of simulation. (b,d) Same as (a,c) but for 500-700 m depths averages. High-melt and low-melt experiments refer to simulations where ice-ocean heat and salt transfer coefficients of Pine Island and Thwaites ice shelves are multiplied by 2 and 0.5, respectively, compared to the control (Ctrl) experiment. The bathymetry contour of 2000 m is shown in black. The dark gray and gray areas represent the grounded ice sheet and floating ice shelves, respectively.

https://doi.org/10.5194/egusphere-2025-5958
Preprint. Discussion started: 3 February 2026

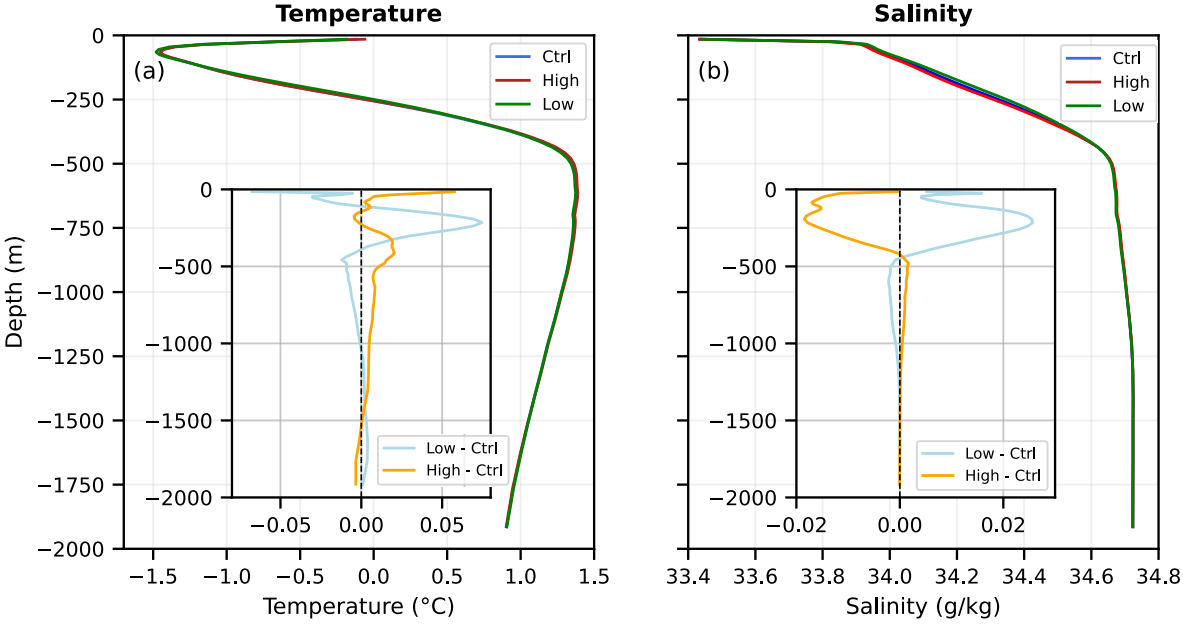

Figure 13. (a,b) Spatially averaged temperature and salinity profiles on the Amundsen continental shelf (between 120°W and 100°W and bathymetry shallower than 2000 m) for high-melt (High), control (Ctrl), and low-melt (Low) experiments, after 5 years of simulation. The sub-panels show the difference in temperature and salinity between the sensitivity experiments (High, Low) compared to the control (Ctrl) experiment. High-melt and low-melt experiments refer to simulations where ice-ocean heat and salt transfer coefficients of Pine Island and Thwaites ice shelves are multiplied by 2 and 0.5, respectively, compared to the control experiment.

https://doi.org/10.5194/egusphere-2025-5958
Preprint. Discussion started: 3 February 2026

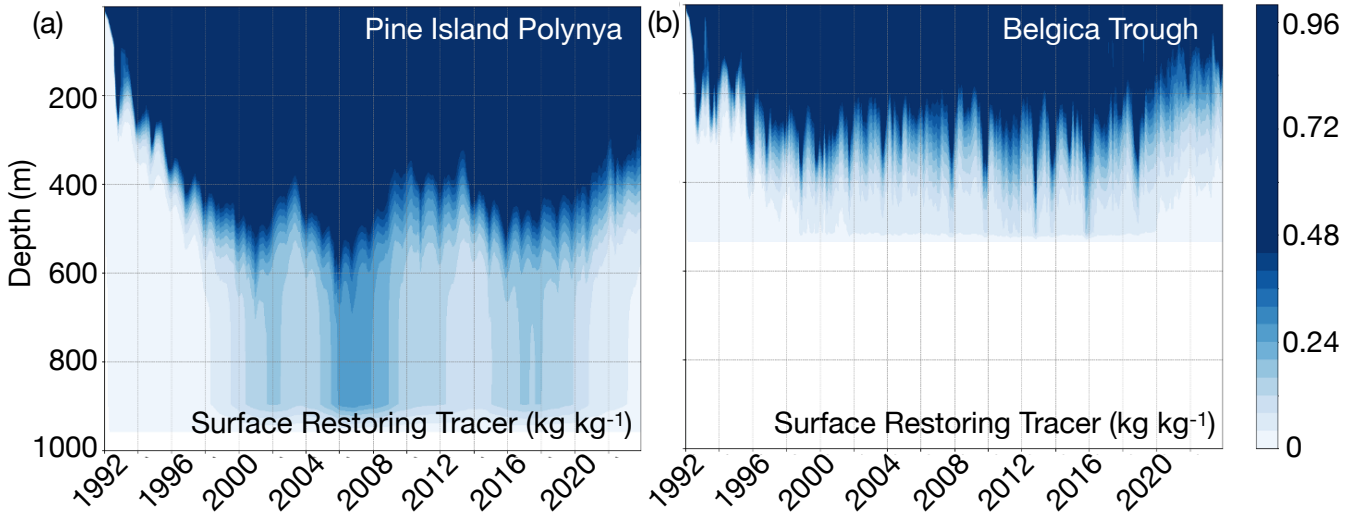

Figure 14. The concentration of a surface restoring tracer in kg of tracer per kg of seawater (kg/kg) situated (a) north of the Dotson Ice Shelf at 73.41 °S and 114.96 °W within the region, typically occupied by deep convection in the Amundsen Sea Polynya, and (b) the Belgica Trough of the Bellingshausen Sea at 73.41 °S and 83.09 °W. These locations are shown with white squares in Figure 1.

https://doi.org/10.5194/egusphere-2025-5958
Preprint. Discussion started: 3 February 2026

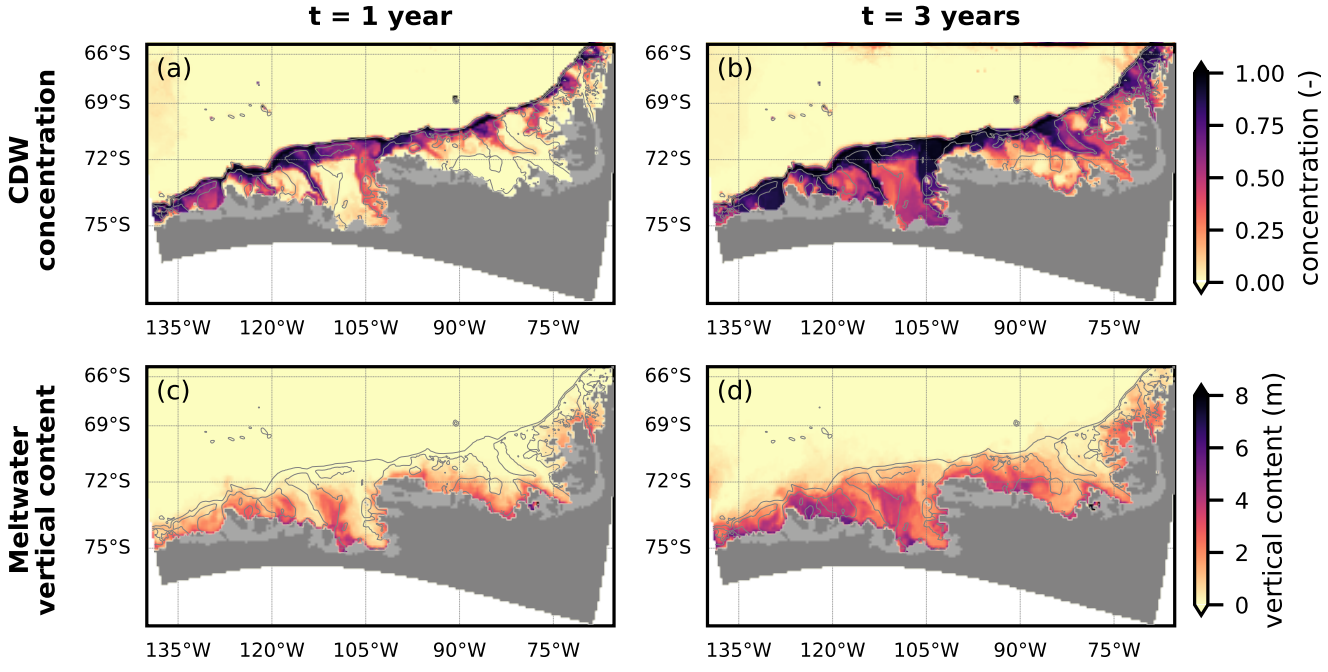

Figure 15. Bottom concentration of tracer representing Circumpolar Deep Water (TR2), that initially lay in front of the continental shelf, after (a) 1 year and (b) 3 years of simulation. Spatial distributions of vertically integrated meltwater content after (c) 1 year and (d) 3 years of simulation. The bathymetry contours of 500 and 2000 m are shown in gray. The dark gray and gray areas represent the grounded ice sheet and floating ice shelves, respectively.

https://doi.org/10.5194/egusphere-2025-5958
Preprint. Discussion started: 3 February 2026

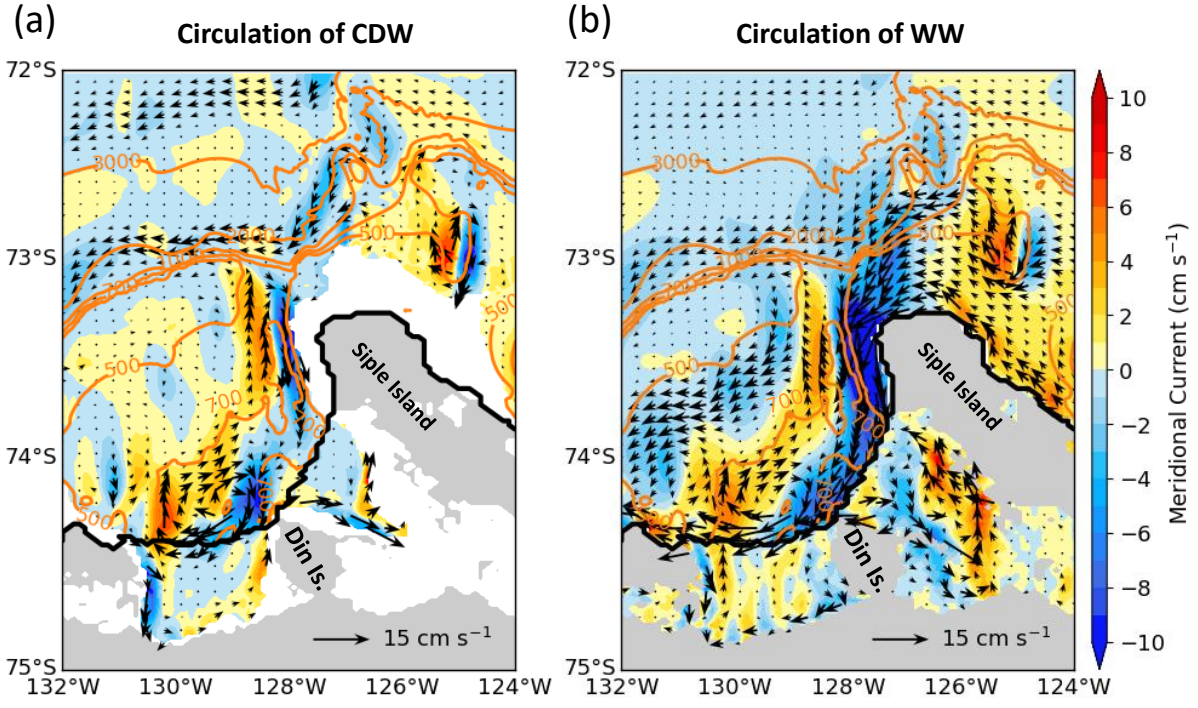

Figure 16. Mean circulation of the (a) lower-layer modified Circumpolar Deep Water (mCDW) and (b) upper-layer Winter Water in the western Getz Ice Shelf region, averaged over 1992–2020. The mCDW layer is defined as the deeper layer below the 0.7 °C isotherm. Meridional velocities are shown in color shading, where positive values indicate northward flow and negative values indicate southward flow. Thick black contours denote the ice-shelf front and the orange line indicates the bathymetry (in meters).

https://doi.org/10.5194/egusphere-2025-5958
Preprint. Discussion started: 3 February 2026

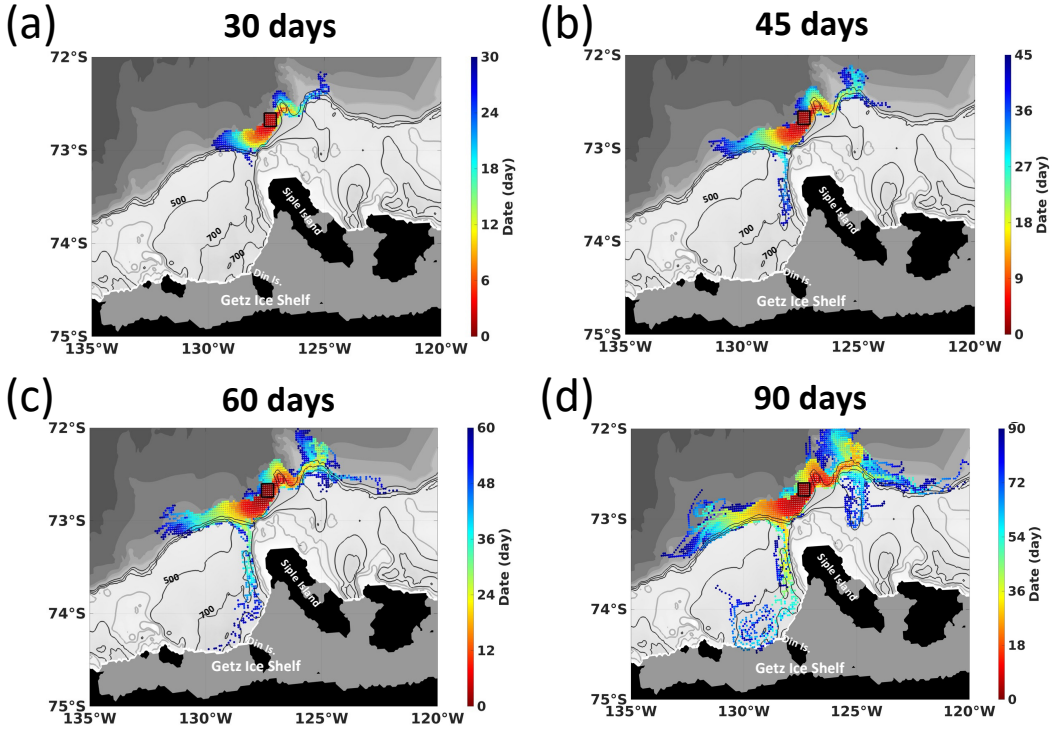

Figure 17. Forward particle trajectories from the source region (black box) with particles released at 600-750 m depth, representing a plausible offshore CDW source region flowing onto the shelf. Trajectories are shown at 30, 45, 60, and 90 days after release on 1 January 2016. Colors indicate particle age (days). Bathymetric contours are shown in meters.

https://doi.org/10.5194/egusphere-2025-5958
Preprint. Discussion started: 3 February 2026

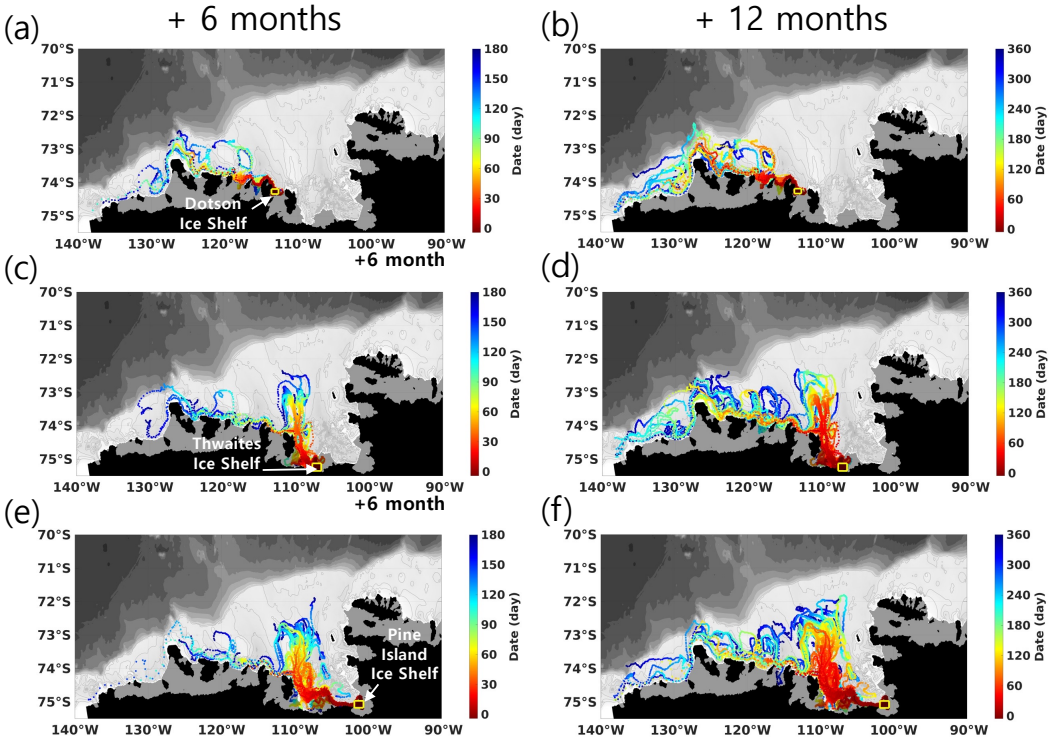

Figure 18. Forward particle trajectories of meltwater released from major ice shelves in the Amundsen Sea. Particles were initialized in the surface grid cells adjacent to the ice fronts of the (a, b) Dotson Ice Shelf, (c, d) Thwaites Ice Shelf, and (e, f) Pine Island Ice Shelf. Trajectories after 6 months (left panels) and 12 months (right panels) illustrate the downstream dispersion pathways. Colors denote the elapsed time since release, and contours indicate the bottom topography.

https://doi.org/10.5194/egusphere-2025-5958
Preprint. Discussion started: 3 February 2026

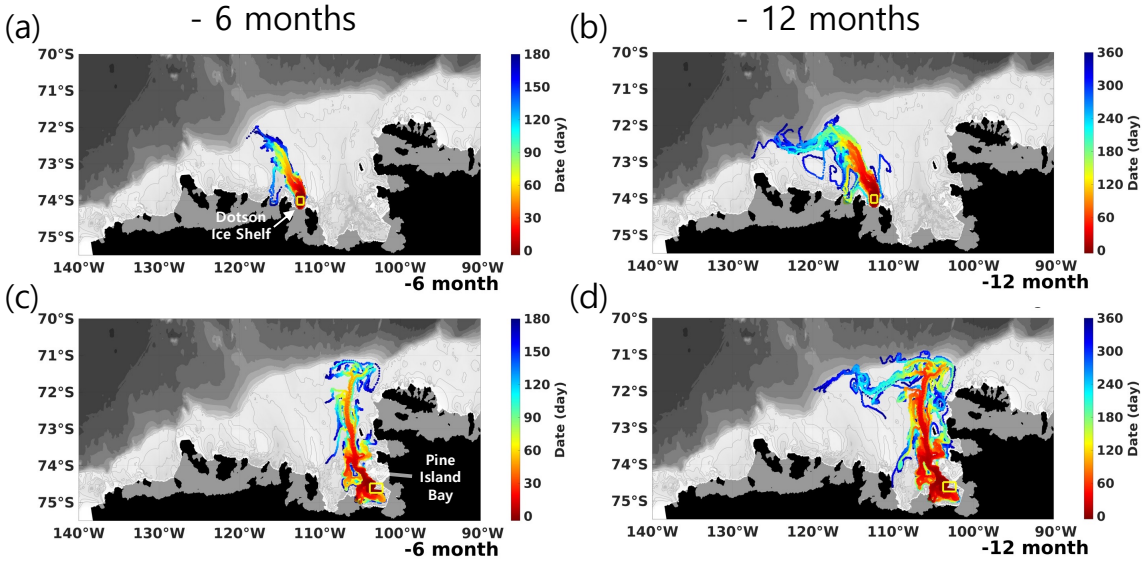

Figure 19. Backward particle-tracking experiments of mCDW in the Amundsen Sea. Particles were released below 700 m in the (a, b) eastern Dotson Trough and (c, d) Pine Island Bay Trough and tracked backward to their source regions. Panels show trajectories over the 6 months (left panels) and 12 months (right panels) preceding arrival, illustrating the dominant mCDW pathways. Colors denote the number of days before arrival at the release sites, and contours indicate bottom topography.

https://doi.org/10.5194/egusphere-2025-5958
Preprint. Discussion started: 3 February 2026

Table 1. Sea ice production in polynyas

	Wrigley Gulf	Amundsen	Pine Island Bay	Bellingshausen
Observertion (km^3 d^{-1})	0.16	0.42	0.17	0.09
Model (km^3 d^{-1})	0.20	0.46	0.57	0.50

https://doi.org/10.5194/egusphere-2025-5958
Preprint. Discussion started: 3 February 2026

Table 2. Comparison of observations with model results for maximum potential temperature and salinity in sections (Figure 1).

	Max Pot.Temperature [°C]		Max Salinity	
Section	Observation	Simulation	Observation	Simulation
Eastern Trough (Jan., 2009)	1.67	1.82	34.73	34.73
Dotson Trough (Feb.-Mar., 2007)	1.38	1.66	34.73	34.73
Dotson Trough (Feb.-Mar., 2012)	1.20	1.65	34.71	34.72
Siple Trough (Mar., 2007)	1.62	1.56	34.73	34.73
Siple Trough (Feb., 2018)	1.52	1.68	34.73	34.73
Western Getz Trough (Mar., 2007)	1.48	1.56	34.73	34.73

Table 3. Comparison of observations with model results for maximum potential temperature and salinity in sections (Figure 1).

	Max Pot.Temperature [°C]		Max Salinity	
Section	Observation	Simulation	Observation	Simulation
Belgica Trough at the shelf break (Mar., 2007)	1.44	1.64	34.73	34.71
Belgica Trough at the shelf break (Dec., 2007 - Jan., 2019)	1.45	1.67	34.72	34.72
Belgica and Latady Troughs (Mar., 2007)	1.44	1.58	34.72	34.70
Belgica and Latady Troughs (Jan., 2019)	1.36	1.57	34.72	34.71

https://doi.org/10.5194/egusphere-2025-5958
Preprint. Discussion started: 3 February 2026

Table 4. Observation-based estimates of basal melt rate (Rignot et al., 2013; Depoorter et al.,2013; Liu et al.,2015; Adusumilli et al., 2020) and model mean basal melt rates for Cosgrove, Pine Island, Thwaites, Crosson and Dotson, and Getz ice shelves in the Amundsen Sea.

Basal melt rate[Gt/yr]	Cosgrove	Pine Island	Thwaites	Crosson and Dotson	Getz
Rignot et al.,2013 (2003-2008)	8.5±2	101.2±8	97.5±7	38.5±4 (Crosson) 45.2±4(Dotson)	144.9±14
Simulation (2003-2008)	12.7±4.7	79.1±11.6	35.6±9.5	44.2±8.5	117.0±18.2
Depoorter et al.,2013 (2007-2009)	11±3	95±14	69±18	78±7	136±23
Simulation (2007-2009)	17.1±1.5	92.7±4.2	44.1±5.3	59.9±5.9	137.7±11.6
Liu et al.,2015 (2005-2011)	8±1	51±8	52±19	37±5	96±16
Simulation (2005-2011)	17.2±2.2	92.9±7.6	44.3±5.4	56.0±9.6	123.7±18.7
Adusumilli et al.,2020 (1994-2018)	2.7±4.1	76.6±8.6	81.9±7.4	20.9±4.9 (Crosson) 28.2±8.5(Dotson)	124.1±40.9
Simulation (1994-2018)	13.3±4.6	85.1±12.6	36.4±9.4	50.7±12.6	127.9±29.6
Adusumilli et al.,2020 (2010-2018)	4.2±4.1	76.0±8.7	81.1±7.4	17.9±4.9 (Crosson) 26.1±8.5(Dotson)	122.6±40.9
Simulation (2010-2018)	14.7±4.2	88.0±14.1	36.9±10.0	51.3±12.8	129.1±29.0

https://doi.org/10.5194/egusphere-2025-5958
Preprint. Discussion started: 3 February 2026

Table 5. Observation-based estimates of basal melt rate (Rignot et al., 2013; Depoorter et al.,2013; Liu et al.,2015; Adusumilli et al., 2020) and model mean basal melt rates for Wilkins, Bach, George VI, Stange, Ferrigno, Venable, and Abbot ice shelves in the Bellingshausen Sea.

Basal melt rate[Gt/yr]	Wilkins	Bach	George VI	Stange	Ferrigno	Venable	Abbot
Rignot et al.,2013 (2003-2008)	18.4±17	10.4±1	89.0±17	28.0±6	5.1±2	19.4±2	51.8±19
Simulation (2003-2008)	40.4±9.2	11.2±1.3	152.7±3.4	29.1±3.6	0.8±0.4	17.5±6.8	54.8±20.8
Depoorter et al.,2013 (2007-2009)	144±42				–	15±3	86±22
Simulation (2007-2009)	34.6±8.0	10.9±1.6	148.0±3.5	24.9±4.0	0.7±0.4	14.0±7.2	63.5±15.8
Liu et al.,2015 (2005-2011)	44±19		15±3(North) 41±10(Sorth)	27±3	21±4	15±2	46±7
Simulation (2005-2011)	36.6±9.5	11.1±1.5	151.6±4.5	26.6±4.9	0.8±0.4	17.4±7.5	61.0±19.7
Adusumilli et al.,2020 (1994-2018)	26.1±32.0	13.1±8.5	88.8±45.7	25.4±14.2	–	14.3±5.5	37.1±38.1
Simulation (1994-2018)	39.5±8.8	11.6±1.6	158.4±7.9	29.3±3.9	0.7±0.4	15.0±7.3	49.4±15.4
Adusumilli et al.,2020 (2010-2018)	23.2±32.0	11.8±8.5	82.4±45.7	25.9±14.2	–	10.3±5.5	37.9±38.2
Simulation (2010-2018)	39.4±10.0	12.0±1.6	161.0±7.1	29.8±4.5	0.8±0.4	15.7±6.8	50.1±11.3

https://doi.org/10.5194/egusphere-2025-5958
Preprint. Discussion started: 3 February 2026

Table 6. 2018-2022 melt rate of Pine Island and Thwaites ice shelves using different ice-ocean heat and salt transfer coefficients. High-melt (low-melt) experiment refers to transfer coefficients multiplied (divided) by 2 compared to the control (ctrl) experiment.

	Low-melt exp.	**Ctrl exp.**	**High-melt exp.**
Pine Island (Gt y^{-1})	53	93	127
Thwaites (Gt y^{-1})	24	43	59